The Signature and Elimination of Sediment Reverberations on Submarine Receiver Functions

Ziqi Zhang[1] and Tolulope Morayo Olugboji[1]

[1]University of Rochester

November 23, 2022

Abstract

While the receiver function technique has been successfully applied to high-resolution imaging of sharp discontinuities within and across the lithosphere, it has been shown, however, that it suffers from severe limitations when applied to seafloor seismic recordings. This is because the water and sediment layer could strongly influence the receiver function traces, making detection and interpretation of crust and mantle layering difficult. This effect is often referred to as the singing phenomena in marine environments. Here, we show how one can silence this singing effect. We demonstrate, using analytical and synthetic waveform modeling, that this singing effect can be reversed using dereverberation filters tuned to match the elastic property of each layer. We apply the filter approach to high-quality earthquake records collected from the NoMelt seismic array deployed on normal, mature (~70 Ma) Pacific seafloor. An appropriate filter designed using the elastic properties of the underlying sediments, and obtained from prior studies, greatly improves the detection of Ps conversions generated from the moho (~8.6 km) and from a sharp discontinuity (<~ 5 km) across the lithosphere asthenosphere transition (~72 km). Sensitivity tests show that the filter is robust to small errors in the sediment properties. Our analysis suggests that appropriately filtering out the sediment reverberations from ocean seismic data could make inferences on subsurface structure more robust. We expect that this study will enable high-resolution receiver function imaging of the base of the oceanic plate across a growing fleet of ocean bottom seismic arrays being deployed in the global oceans.

The Signature and Elimination of Sediment Reverberations on Submarine Receiver Functions

Ziqi Zhang[1*], and Tolulope Olugboji[1]

[1] *Department of Earth and Environmental Sciences, University of Rochester, NY*

Corresponding author: Ziqi Zhang (ziqi.zhang@rochester.edu)

Key Points:

- A dereverberation filter is proposed to eliminate the sediment reverberation effects on receiver functions of OBS data.
- The proposed filter is proven effective and robust to small errors in sediment properties using synthetic modeling.
- A Moho of 8.6 km depth and a sharp discontinuity of the lithosphere asthenosphere transition of 72 km depth is observed.

Abstract

While the receiver function technique has been successfully applied to high-resolution imaging of sharp discontinuities within and across the lithosphere, it has been shown, however, that it suffers from severe limitations when applied to seafloor seismic recordings. This is because the water and sediment layer could strongly influence the receiver function traces, making detection and interpretation of crust and mantle layering difficult. This effect is often referred to as the singing phenomena in marine environments. Here, we show how one can silence this singing effect. We demonstrate, using analytical and synthetic waveform modeling, that this singing effect can be reversed using dereverberation filters tuned to match the elastic property of each layer. We apply the filter approach to high-quality earthquake records collected from the *NoMelt* seismic array deployed on normal, mature (~70 Ma) Pacific seafloor. An appropriate filter designed using the elastic properties of the underlying sediments, and obtained from prior studies, greatly improves the detection of Ps conversions generated from the moho (~8.6 km) and from a sharp discontinuity (<~ 5 km) across the lithosphere asthenosphere transition (~72 km). Sensitivity tests show that the filter is robust to small errors in the sediment properties. Our analysis suggests that appropriately filtering out the sediment reverberations from ocean seismic data could make inferences on subsurface structure more robust. We expect that this study will enable high-resolution receiver function imaging of the base of the oceanic plate across a growing fleet of ocean bottom seismic arrays being deployed in the global oceans.

1.0 Introduction

The seismic structure of the normal oceanic lithosphere-asthenosphere system is pivotal to our understanding of global geodynamics and plate tectonics (Kawakatsu & Utada, 2017; Olugboji, Park, Karato, et al., 2016; C. Rychert et al., 2020; C. A. Rychert et al., 2018b). For instance, understanding how seismic velocities are affected by temperature, melt or attenuation, can shed light on how the oceanic plate evolves and what the likely causes are for the rheological transition from a rigid lithosphere to a weak asthenosphere (Karato, 2012; Kawakatsu et al., 2009; Ma et al., 2020; Olugboji, Park, & Karato, 2016; C. Rychert et al., 2020). While multiple seismic techniques (e.g., surface waves, SS precursors, Ps and Sp converted waves, etc.) are often unanimous about the presence of a high velocity lithospheric lid underlain by a low velocity asthenosphere interior, these techniques have different resolution and sensitivities to the sharpness of the velocity gradient (Eaton et al., 2009; Olugboji et al., 2013) and, therefore, need to be used in a complementary manner.

The new seismic profiles derived from the higher resolution body-wave techniques differ from the early studies from surface waves, in that they identify a sharp and distinct seismic discontinuity across the thermal boundary layer, suggesting modifications to the simple plate-cooling models (Karato & Park, 2018; Kawakatsu & Utada, 2017; C. A. Rychert et al., 2018a). One scenario invokes a unique role for partial melting and anisotropy (Hirschmann, 2010; Kawakatsu et al., 2009; C. A. Rychert et al., 2018a), while another seeks to explain these observation using a sub-solidus attenuation mechanism (Karato & Park, 2018; Olugboji et al., 2013; Olugboji, Park, Karato, et al., 2016) to explain a sharp and large velocity reversal that can be age dependent. A systematic receiver function study of normal oceanic mantle at various seafloor ages seems to support the latter view: an observed age-dependence in sharpness and depth for the oceanic mantle especially where no azimuthal dependence in seismic velocities (Olugboji, Park, Karato, et al., 2016).

In principle, the receiver function technique should provide the best resolution on the age-dependence, depth, and sharpness of a sharp velocity gradient, making it a promising seismic technique for investigating the lithosphere structure of an oceanic plate (Akuhara et al., 2016, 2017; Akuhara & Mochizuki, 2015; Audet, 2016; K. Hannemann et al., 2017; Janiszewski & Abers, 2015; Kawakatsu et al., 2009; P. Kumar et al., 2011; Liu et al., 2020; Olugboji, Park, Karato, et al., 2016; C. a. Rychert et al., 2013; C. A. Rychert et al., 2018a). However, it has been pointed out that in the seafloor environment they can be complicated by sediment reverberations and should be treated with caution (Audet, 2016; Kawakatsu & Abe, 2016; Olugboji, Park, & Karato, 2016).

The challenge of interpreting the receiver functions using seafloor seismic data results from near-surface reverberations obscuring weaker conversions from deeper crust and mantle discontinuities, making structural inference unreliable (Audet, 2016). The scattered wavefield trapped in the overlying water column and the soft sediment layer generate a loud ringing in receiver function traces, a behaviour that is very pronounced for sediment layers which generate resonance modes at high frequencies, e.g., along the coastal plain or in slow shear-wave sediments. While techniques for removing the water reverberations have long been studied in marine environments (Backus, 1959), and by applying a wavefield decomposition approach (Bostock & Trehu, 2012; Osen et al., 1999; Thorwart & Dahm, 2005), only recently has the water-filter approach been applied to the source-deconvolved receiver function traces aiding interpretation of ocean lithospheric structure (Akuhara et al., 2016, 2017; Akuhara & Mochizuki, 2015). These techniques have focused on removing water-column reverberations, and while the filters are easy to design, no study has yet been applied to removing the sediment reverberations in the deep ocean environments, even though similar techniques have been applied to suppressing sediment reverberations observed on receiver functions obtained from continental seismometers (Cunningham & Lekic, 2019; Yu et al., 2015).

In this study, we generalize the inverse-water filter approach used in (Akuhara & Mochizuki, 2015; Backus, 1959) to design a two-stage filter that suppresses both the water-column and sediment-layer reverberations, the latter being more severe in its effect on receiver function analysis (Audet, 2016; K. Hannemann et al., 2017; Katrin Hannemann et al., 2016; Kawakatsu & Abe, 2016; Olugboji, Park, & Karato, 2016). By using synthetic wavefield modeling, we demonstrate that an appropriate dereverberation filter for removing offending reverberations can be designed by tuning to the relevant elastic properties of the sediment layer, i.e., thickness and shear velocity contrast at the sediment-crust interface. The filter is prescribed completely by the two-way travel times and the reflectivity of the water-sediment or the sediment-crust interfaces (Aki & Richards, 2002). We describe why this approach is preferred to the empirical procedure of using the autocorrelation of the receiver functions used with continental seismometers (Cunningham & Lekic, 2019; Yu et al., 2015).

We illustrate our methodology by designing an appropriate dereverberation filter for receiver functions, calculated using ocean bottom seismological (OBS) data, obtained from the *NoMelt* experiment located on mature (~70Ma) Pacific seafloor. We describe how the receiver function results obtained after application of the filter show that the sedimentary layer reverberations can be successfully attenuated and the interpretation of deeper crust or lithospheric layering improved. We compare our high-frequency receiver function results with previous body wave (Gaherty et al., 1996; Tan & Helmberger, 2007), attenuation (Ma et al., 2020) and conductivity constraints (Sarafian et al., 2015) in the NoMelt region, and discuss its implication for models of oceanic lithosphere asthenosphere structure (Karato & Park, 2018; Olugboji et al., 2013; C. Rychert et al., 2020).

2.0 Receiver Function for Deep Seafloor Seismometers

Receiver functions (RFs) are aptly named because they recover receiver-side structure underneath a seismic station after the source and path effects have been removed following either the deconvolution of the horizontal waveform by the vertical waveform (Ps-RFs) or vice-versa (Sp-RFs) (Bostock, 2004; Rondenay, 2009). In the marine environment, even after the source effects have been removed, the strong influence of the sediments beneath the receiver may still obscure interpretation of deeper receiver-side structure (Kawakatsu & Abe, 2016). In this section, we describe the behavior of each reverberation layer and how their effects can be removed from the receiver function traces by a matched dereverberation filter.

A successful application of the dereverberation filter can be judged by how well the response of the crust and mantle layering can be recovered from the filtered RFs. We do this by using a parameter search based on correctly predicting the travel times and relative amplitudes of the appropriate scattered phases. In the deep marine environments, we show that knowledge of the elastic properties of the sediments is key to recovering crust and mantle layering.

2.1 Identifying and Removing Water and Sediment Resonances

The significance of reverberations generated in the offshore environment, from an ocean water column and sedimentary layer, have long been recognized as one of the most challenging factors that hamper investigating deeper crustal and mantle structures using ocean bottom seismometer data (Backus, 1959; Godin & Chapman, 1999; Kawakatsu & Abe, 2016). In the shallow offshore environment, the reverberation from the ocean water column traps seismic waves while they are reflected at both the sea surface and the seafloor, causing the vertical component records of the OBSs to be masked by the water reverberations (Akuhara & Mochizuki, 2015; Audet, 2016). When pressure data is available, this can be used to suppress the water layer conversions using a wavefield decomposition approach (Bostock & Trehu, 2012; Osen et al., 1999; Thorwart & Dahm, 2005). Previous studies have shown that the effects of the water column are not severe in the deep marine waters since the water reverberations arrive later in the P coda (Audet, 2016), however, they may still interfere with signals from deeper velocity discontinuities, e.g., lithosphere-asthenosphere boundary (LAB). Additionally, a thin layer of pelagic or terrigenous sediments in such an environment could render receiver functions almost uninterpretable.

Our goal in this work is to suppress the negative effects of these reverberations on the receiver function traces, using a technique similar to an idea that is well-documented on land-based seismic stations (Cunningham & Lekic, 2019; Yeck et al., 2013; Yu et al., 2015). For an oceanic model with a low-velocity sedimentary layer or water column (Figure 1), the receiver function (the source-deconvolved seismograms) can be expressed as:

$$R(t) = \sum_{n=0}^{\infty} (-r_0)^n \widetilde{R}(t - n\Delta t) \tag{1}$$

where R and $\widetilde{R}$ are the receiver functions with and without the influence of sedimentary layer or water column, respectively, r_0 is the reverberation strength, and Δt is the two-way travel time of the reverberated S waveleg within the sediment layer (or reverberated P waveleg within the water layer).

In the frequency domain, equation (1) can be expressed as (Backus, 1959; Snieder & Snieder, 2001):

$$R(f) = \widetilde{R}(f) \sum_{n=0}^{\infty} (-r_0)^n e^{-i2\pi f n\Delta t} \tag{2}$$

Notice that $\sum_{n=0}^{\infty}(-r_0)^n e^{-i2\pi f n\Delta t}$ is a geometric series that can be simplified as $(1+r_0 e^{-i2\pi f\Delta t})^{-1}$, which allows us to write the infinite series as a linear filter in the frequency domain that causes a reverberation effect:

$$R(f) = \widetilde{R}(f) \cdot E(f) \quad \textbf{(3a)}$$

$$\widetilde{R}(f) = R(f) \cdot F(f) \quad \textbf{(3b)}$$

$$F(f) = E^{-1}(f) = (1 + r_0 e^{-i2\pi f \Delta t}) \quad \textbf{(3c)}$$

where E is the reverberation effect of the sediment or water layer, and F is the reverberation removal filter in the frequency domain, which eliminates the appropriate resonance caused by waves trapped in a water or sediment layer (notice that $E \cdot F = 1$).

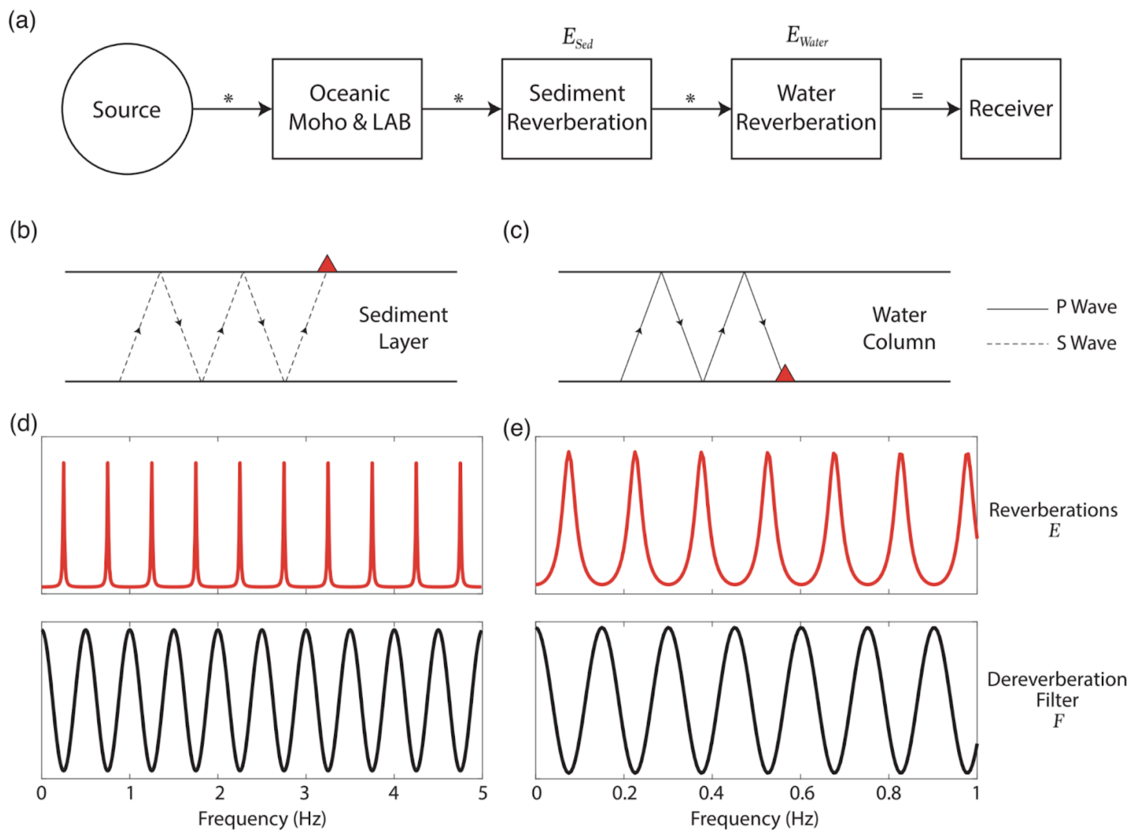

Figure 1. Systematic description of the reverberations and the dereverberation filter design. (a) Wave paths of teleseismic events when sediment and water are present. (b) Sketches of S wavelegs traveling in the sediment layer causing reverberations. The red triangle denotes the station. (c) Sketches of P wavelegs traveling in the water column causing reverberations. (d) Sedimentary reverberation effects E_{Sed} (top) and the corresponding dereverberation filter F_{Sed} (bottom) in the frequency domain. (e) Same as Figure 1d but for water reverberations E_{Water} and the corresponding filter F_{Water}.

A few points can very quickly be summarized about the reverberation effect and the corresponding matched dereverberation filters. First, both the sediment and water reverberations have the same form in the frequency domain and behave as comb filters with sharp peaks at the fundamental and overtone frequencies, which are odd multiples of the inverse of the two-way travel time in the respective layer. Second, to suppress the reverberation effect, the matched dereverberation filter is the appropriately scaled notch filter that removes the frequencies at which the reverberations obscure the subsurface conversions. Finally, in the global oceans, the sediment and water-column properties (velocity and thickness) vary in a predictable manner that enables us to judge their relative influence and frequency-dependence. Along the continental shelf, the water column is thin and sediments are thick, while in the deeper oceans, the case is reversed; the water column is deep and the sediments reach some terminal thickness. Since the fundamental frequency of the resonance is governed by the two-way travel in the relevant layer, it is clear that for deep oceans these frequencies are at the low-frequency end of the spectrum (Figure 1e), while the thin sediments have a higher resonance frequency (Figure 1d), which makes the removal of the sediment reverberations crucial in the deep oceans, especially if fine-scale crust and mantle layering is desired using high-frequency (~ 1Hz) receiver functions (Olugboji et al., 2013).

In the application to land-based seismometers presented in Yu et al., (2015), the two parameters of the dereverberation filter (r_0 and Δt) can be estimated empirically from the receiver function data by finding the best-fitting decaying sinusoid to the autocorrelation function of the original receiver function in the time domain (Cunningham & Lekic, 2019):

$$m(t) = R(t) \star R(t) \approx ce^{-at}cos(\frac{\pi t}{\Delta t}) \quad \textbf{(4)}$$

where t is the lag time of the autocorrelated RF, Δt is the half-period of the oscillation, c is the autocorrelation amplitude at zero lag time, and a is the decay constant. Because the half-period of the oscillation is precisely the travel time of the S reverberation, $r_0 = m(\Delta t)$, the parameters of the dereverberation filter can be estimated by fitting this autocorrelation function. In our synthetic tests and marine data examples, we show that Δt and fundamental frequency, f_0 , may be used in conjunction with *PbS* delay time from waveform records, to jointly constrain the allowable range for the sediment velocity and thickness. In the case of sediment reverberations, once the sediment properties are known, the filter can be computed using the reflection coefficient (reverberation strength) and delay time (derived from velocity and thickness of sediments).

To demonstrate this, we compute synthetic receiver functions for two different oceanic plate models, M1 and M2, which highlight the different signatures of a water and sediment layer on receiver function deconvolution (Figure 2a). In this implementation, we demonstrate how the dereverberation filter is used to improve the detection of crust and upper mantle interfaces. We point out that the filter parameters can be derived from the reflection coefficients and two-way travel time for the shear (sediment) and compressional wave (water) reverberations. For ocean bottom data, the appropriate reflection coefficients is for a water layer over halfspace, where water reverberations are suppressed using an r_0 defined by the P-to-P reflection coefficient, R_{PP}, at the sea floor; whereas r_0 is the S-to-S reflection coefficient, R_{SS}, for sediment reverberations (see Text S1-A in Supporting Information for the analytical expressions). The two-way travel times are described by :

$$\Delta t(p_i) = \frac{2H}{v}\sqrt{1 - v^2 p_i^2} \qquad \textbf{(5)}$$

where H and v are the thickness and shear velocity of the sediment layer (or the depth and P velocity of the water column), respectively; and p_i denotes the ray parameter.

Table 1. Density, velocity, and thickness parameters of various layers in the synthetic velocity models.

Layer	ρ (kg/m^3)	Velocity (km/s)		Velocity Ratio	Thickness, H (km)	
		v_p	v_s	κ	M1	M2
Water	1027	1.50	-	-	5.0	5.0
Sediment	2000	2.00	0.50	4.00	-	0.8
Crust	2800	6.50	3.65	1.78	7.0	7.0
*UMM	3300	8.10	4.50	1.80	50.0	50.0
Asthenosphere	3200	8.10	4.10	1.98	-	-

*UMM = UpperMost Mantle;
$\rho_{w,s,c,m,hs}$: the density of water, crust, mantle, and halfspace;
$v_{p,s}$: P-wave and S-wave velocity respectively;
$\kappa = v_p/v_s$: the P to S velocity ratio.

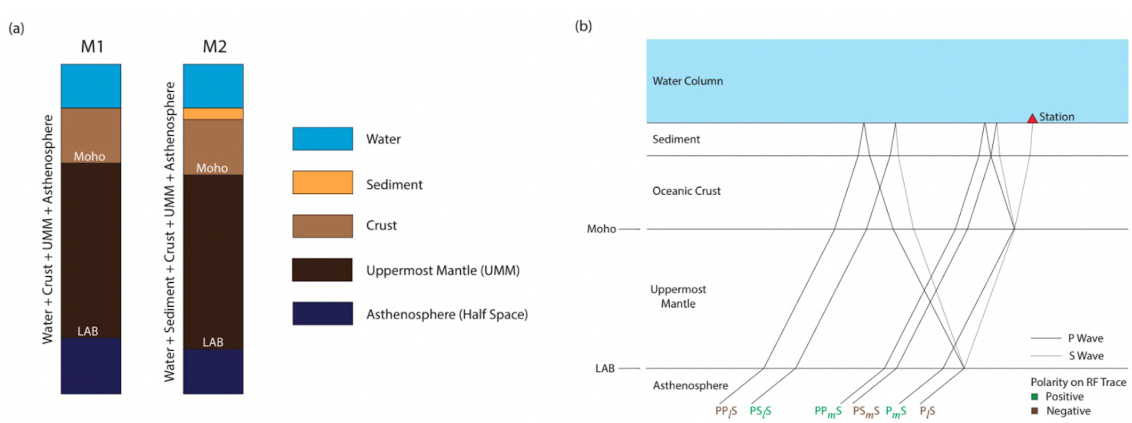

Figure 2. Sketch of velocity models and Ps phases. (a) Representative velocity models used to demonstrate RF estimation in a deep-ocean environment. Model M1 depicts an oceanic crustal and

upper mantle structure with no sediments. Model M2 adds a thin sedimentary layer on top of the oceanic crust in Model M1. Detailed model parameters are shown in Table 1. (b) Schematic diagrams showing the main Ps phases and their multiples from both Moho and LAB, using layered model M2 described in Figure 2a. The names of the phases are labeled next to each ray path; green and brown names indicate positive and negative polarities on the RF traces, respectively.

2.2 Recovery of Crust & Mantle Layering: RF Interpretation

Successful application of a reverberation filter can be assessed by how well the receiver function traces can be interpreted for the appropriate Ps conversions and multiples. We model the phase-delay time using a grid search stacking approach to estimate the thickness (H), and P-to-S wave velocity ratio (κ), independent of the P velocity (Vp) (Bostock & Kumar, 2010; Helffrich & Thompson, 2010; M. R. Kumar & Bostock, 2008). This requires predicting the travel times of converted and reflected phases within a particular multi-layered model. For example, in a traditional grid search (Zhu & Kanamori, 2000), the travel times of the P-to-S converted phase and its reverberations for a single crustal layer at the Moho are given by:

$$t_{P_mS} = \frac{H}{v_p}\left(\sqrt{\kappa^2 - p_i^2 v_p^2} - \sqrt{1 - p_i^2 v_p^2}\right), \tag{6a}$$

$$t_{PP_mS} = \frac{H}{v_p}\left(\sqrt{\kappa^2 - p_i^2 v_p^2} + \sqrt{1 - p_i^2 v_p^2}\right), \tag{6b}$$

$$t_{PS_mS} = \frac{2H}{v_p}\sqrt{\kappa^2 - p_i^2 v_p^2}. \tag{6c}$$

We can write this in a compact fashion using the following substitutions: $A = \sqrt{\kappa^2 - p_i^2 v_p^2}$ and $B = \sqrt{1 - p_i^2 v_p^2}$. A close observation shows that the travel time ratios can be written independent of thickness H, which makes it possible to write the travel time of the multiples (t_{PP_mS} and t_{PS_mS}) in terms of the primary conversion phase t_{P_mS}:

$$t_{PP_mS}(p_i) = \frac{A+B}{A-B} t_{P_mS}(p_i), \tag{7a}$$

$$t_{PS_mS}(p_i) = \frac{2A}{A-B} t_{P_mS}(p_i). \tag{7b}$$

Since the direct conversion is typically the earliest and strongest arrival, it is easily identified in the receiver function traces; moreover, for a thin crust, it exhibits minimal moveout compared to the reference phase (zero lag RF). Therefore, we can constrain $t_{P_mS}(p_i)$ by estimating the maximum RF amplitude within an expected arrival window (e.g., around 1s for model M1). With a clear observation for $t_{P_mS}(p_i)$ estimated from the RF traces, the other parameters, κ and v_p, are obtained by stacking the RFs along the travel time trajectories for the other multiples (i.e., equation (7)). The stack is described using a 2-D grid search for $\hat{\kappa}$ and $\hat{v_p}$:

$$s = \sum_i \sum_j w_j G(t_{ij}) R_j(t) \tag{8}$$

where s is the stacking amplitude, t_{ij} is the predicted travel time of the jth phase used (i.e. t_{P_mS}, t_{PP_mS}, t_{PS_mS}) based on the estimated *PmS* arrival described in equation (7), $G(t)$ is a gaussian smoothing window centered at time t, $R_j(t)$ is the jth radial receiver function trace, and w_j is the weighting factors for different phases based on the amplitudes and polarities calculated from the transmission and reflection coefficients provided in Table 2. Consequently, the optimal pair of $\hat{\kappa}$ and $\hat{v_p}$ is obtained when the stacking amplitude, s, reaches maximum.

Table 2. Polarities and amplitudes of Ps conversion phases and their multiples, from Moho and LAB.

	M1			M2		
Phase	Amplitude	Weight (w_i)	Polarity	Amplitude	Weight (w_i)	Polarity
PmS	0.1632	44.76%	+	0.2885	64.61%	+
PPmS	0.1054	28.91%	+	0.1510	33.81%	+
PSmS	-0.0960	-26.33%	-	-0.0070	-1.57%	-
PlS	-0.0735	-60.29%	-	-0.1300	-72.79%	-
PPlS	-0.0331	-27.18%	-	-0.0475	-26.59%	-
PSlS	0.0153	12.53%	+	0.0011	0.63%	+

*The lowercase *m* and *l* in the names of the phases denotes conversions at Moho and LAB. The ray paths of the phases are shown in Figure 2b. Amplitudes and weights are calculated using relevant reflection and transmission coefficients for an incoming P wave with a ray parameter of 0.08 (see Text S1-B in Supporting Information for details on calculation).

The first stack uses the set of travel times described in equation (7) that are independent of layer thickness, while a second stage stack proceeds by performing a 1-D line search for optimal layer thickness $\hat{H}$, using equation (8), with the new predicted travel times for the primary phase and multiples, after substituting κ and v_p in equation (6) with the optimal $\hat{\kappa}$ and $\hat{v_p}$ obtained from the first stack.

It is easy to generalize this procedure for estimating the depth of a prominent lithospheric discontinuity (LAB depth). In this case, we assume that the mantle velocities ($\hat{\kappa}_m$, $\hat{v}_{pm}$) are relatively well constrained, either from PREM, AK135 or a regional oceanic velocity model (Dziewonski & Anderson, 1981; Kennett et al., 1995; C. A. Rychert et al., 2018b). The stack described in equation (8) is then implemented to perform a 1-D line search for the

Moho-LAB thickness, where t_{ij} is now the predicted travel times of the LAB-associated phases, i.e., *PlS* and *PPlS*:

$$t_{P_lS}(p_i) = \hat{t'}_{P_mS}(p_i) + \frac{H_{LAB}}{\hat{v}_{p_m}}(\hat{A}_m - \hat{B}_m) \tag{9a}$$

$$t_{PP_lS}(p_i) = \hat{t'}_{P_mS}(p_i) + \frac{H_{LAB}}{\hat{v}_{p_m}}(\hat{A}_m + \hat{B}_m) \tag{9b}$$

where $\hat{A}_m = \sqrt{\hat{\kappa}_m^2 - p_i^2 \hat{v}_p{}^2}$ and $\hat{B}_m = \sqrt{1 - p_i^2 \hat{v}_p{}^2}$; $\hat{t'}_{P_mS}$ is the predicted travel time of the *PmS* phase calculated from equation (6a) using optimal $\hat{\kappa}$, $\hat{v}_p$ and $\hat{H}$ from the Moho stack.

We note that since percent velocity change at the LAB is not as large as the Moho, the amplitudes of the reflected multiples may be insignificant. A comparison of the relative amplitude of the main Ps phases from both Moho and LAB, using velocity model M2 (Table 2), shows that the relative amplitude of the second multiple from the LAB (PS_lS) is very minimal, which is why we only use the *PlS* and *PPlS* phases (i = 1, 2 in equation (8)). In the presence of thin sediments, these travel time equations need to be adjusted (see Text S2 in Supporting Information for the appropriate time corrections in the presence of sediments).

3.0 Synthetic Tests

We present the successful application of our dereverberation filter to receiver function traces computed using oceanic velocity models, in the presence of a water layer (M1) and both water layer and sediment layer (M2). The receiver functions are generated using reflectivity techniques and when the correct dereverberation filter is applied, the faithful recovery of crust and lithospheric layering is drastically improved.

3.1 Deep Ocean Model - No sediments (M1)

We compute synthetic receiver function traces at teleseismic distances for the oceanic model without sediments (M1). All major phases representing conversions and multiples from the Moho, the seismic LAB, and a first water arrival, can be clearly identified and predicted using the travel time equations (Figure 3a). The oceanic crustal P velocity and P-to-S velocity ratio are accurately predicted using the 2-D ($\kappa - v_p$) grid search (Figure 3b). Crustal thickness is also recovered by the 1-D line search (Figure 3c). The predicted values for κ, v_p, H_m are 1.78, 6.5 km/s and 7.0 km, respectively, which are identical to the input model parameters for M1 (see Table 1). The 1-D line search correctly predicts the depth of the 57 km - deep seismic LAB (Figure 3d) in the presence of a closely overlapping water multiple (see Figure 3a). In the LAB recovery test, we fix the mantle P velocity (8.1 km/s) and P-to-S velocity ratio (1.80) and show that the stack can recover the input values. We then show that slight errors in the mantle v_p or κ result in only a slight error in the predicted depth. For example, a 5% error in v_p (~0.4 km/s) would result in an error of about 3% (~2 km) in the seismic LAB depth (Figure 3e). This bias is within the uncertainties in our measurements.

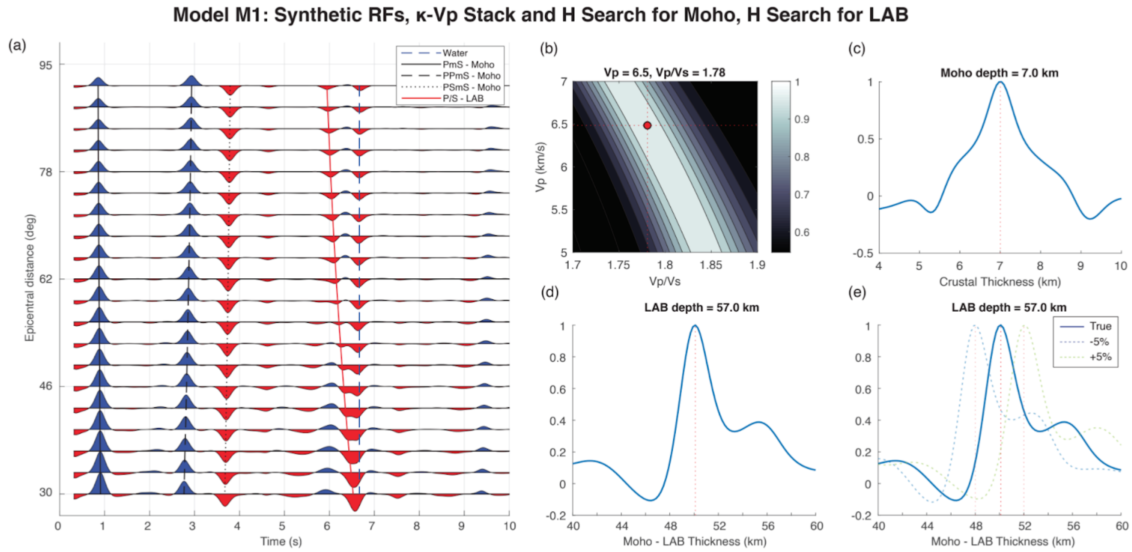

Figure 3. Synthetic receiver function traces and parameter search showing recovery of oceanic velocity model M1. (a) RF traces plotted against epicentral distance. The predicted arrival times for direct Ps conversions and multiples from the Moho are marked as black solid, dashed and dotted lines, respectively; Ps conversion from the LAB is marked as red solid line; the first water reverberation is marked as blue dashed line. (b) $\kappa - v_p$ stack for Moho. (c) Linear search for the depth of Moho. (d) Linear search for the Moho-LAB thickness given the true κ and v_p from the velocity model (see Table 1). (e) Sensitivity of H_{LAB} to uncertainties in mantle velocities. The blue solid line is the same as in Figure 3d; blue and green dashed lines indicate linear search for the Moho-LAB thickness given positive (+5%) and negative (-5%) changes in v_p (relative to the true value defined in Table 1) with fixed true κ.

3.2 Deep Ocean Model in the Presence of Sediment (M2)

In the presence of a sedimentary layer (M2), the unfiltered synthetic receiver function traces display many more phases, the strongest being the pair of reverberations within the sediment layer (~4 - 5s and 8 - 9s). For comparison, we show the predicted timing of the Ps conversion from the Moho, LAB, water and sediment reverberations (Figure 4a). These RF traces are calculated at a high cutoff frequency of 4 Hz, to better identify the phases and demonstrate the effectiveness of the dereverberation filter. Unlike M1, the first positive peak at ~1.2 s is the Ps conversion from the bottom of sediment (*PbS*), while the second positive peak at ~2 s is the direct conversion from the Moho (*PmS*), both of which are clearly identified and separated. The first moho multiple is only slightly detectable in the RF traces at ~4.8 s (*PPmS*), since the nearby sediment reverberations are dominant. This creates a difficult situation with any stack for crustal velocity or thickness. The second moho multiple (*PSmS*) is even more difficult to detect and is barely identifiable due to its low amplitude (see Table 2). Like the direct moho phase, the conversion from the seismic LAB (*PlS*) is also masked by the second set of sediment reverberations (~8 s) and is hardly detectable. Figure 4c-e shows the preliminary stack using these unfiltered traces. Compared to the true values, the predicted crustal P velocity (6.0 km/s), P-to-S velocity ratio (1.83), thickness (6.1 km), and LAB depth (61.4 km) have an error of about 8% (see Table 1).

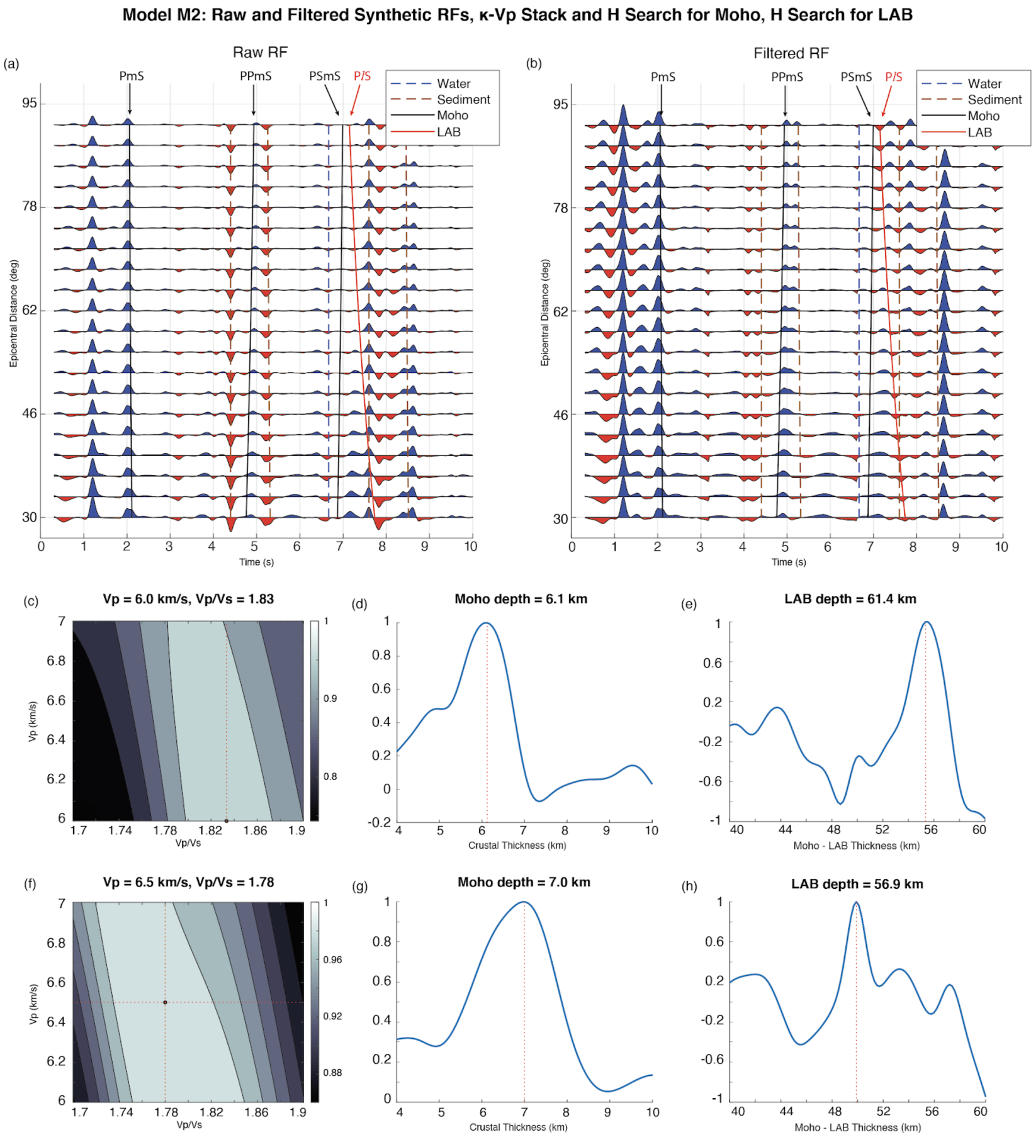

Figure 4. Synthetic receiver function traces and parameter search showing recovery of oceanic velocity model M2. (a) Raw RF traces plotted against epicentral distance. The predicted arrival times for direct Ps conversions and multiples from the Moho are marked as black solid, dashed and dotted lines, respectively; Ps conversion from the LAB is marked as red solid line; the reverberations from the bottom of sediment are marked as brown dashed lines; the first water reverberation is marked as blue dashed line. (b) Filtered RF traces plotted against epicentral distance. The predicted travel times for different phases are marked the same as Figure 4a. (c) $\kappa - v_p$ stack for Moho, using raw RF shown in Figure 4a. (d) Linear search for the depth of Moho, using raw RF shown in Figure 4a. (e) Linear search for the Moho-LAB thickness given the true κ and v_p from the velocity model (see Table 1), using raw RF shown in Figure 4a. (f) $\kappa - v_p$ stack for Moho, using filtered RF shown in Figure 4b. (g) Linear search for the depth of Moho, using filtered RF shown in Figure 4b. (h) Linear search for the Moho-LAB thickness given the true κ and v_p from the velocity model (see Table 1), using filtered RF shown in Figure 4b.

After the synthetic receiver function traces are filtered using the two-stage dereverberation filters (Figure 4b), the reverberations are suppressed and the identification of the moho multiple and LAB conversions are improved. The first and strongest moho multiple, *PPmS*, which was previously masked by the sediment reverberations, is now visible (~4.8 s). The reverberations have been effectively removed, which guarantees that the Moho stack will be reliable. There is also a significant improvement in the seismic LAB conversion (compare *PlS* in Figure 4a and 4b), since with sediment reverberations effectively removed, the *PlS* phase can be clearly identified with the correctly predicted positive travel time moveout. We show substantially improved results after applying the appropriate filter, using the $\kappa - v_p$ stack and H search for Moho, and H search for LAB, respectively (compare Figure 4f-h and 4c-e). With clearly identifiable phases, the stacking results are much more reliable and accurate. The resulting crustal P velocity (6.5 km/s), P-to-S velocity ratio (1.78), thickness (7.0 km), and LAB depth (56.9 km) are nearly identical to the input velocity model (compare errors from unfiltered to filtered).

4.0 Real Data Examples: NoMelt Experiment

We use data recorded by the NoMelt experiment, which was deployed on a mature (~70 Ma) Pacific sea floor, southeast of Hawaii, between the Clarion and Clipperton fracture zones (Figure 5a), from December 2011 to December 2012. The experiment consisted of broadband OBS deployment (Lin et al., 2016; Ma et al., 2020; Russell et al., 2019), an active source experiment (Mark et al., 2019), and a magnetotelluric survey (Sarafian et al., 2015). We process the broadband OBS data and use teleseismic events with magnitudes larger than Mw6.0, located 20 to 150 degrees away from the center of the seismic array (Figure 5b). Within the one-year deployment period, over 120 such earthquakes were recorded by each of the 16 stations.

Ocean Bottom Seismometers are deployed remotely and without intervention, which means, unlike seismometers on land, their actual horizontal orientation on the seafloor is unknown. We used the reported azimuth angle from previous Rayleigh wave analysis (Adrian K. Doran & Laske, 2017; Russell et al., 2019) to rotate the original seismograms to the correct ZRT directions (see Figure 6).

To ensure robust receiver function calculations, we select the earthquake records by applying an SNR (Signal-to-Noise Ratio) based quality check (QC) procedure (Figure 6). This QC procedure measures the SNR of the bandpassed waveforms, and selects the events with SNR > 2.0 on the vertical channel. We observe that the signal quality of the vertical seismograms is degraded because of the sediment resonance which is sometimes visible as a beating phenomenon (Figure 6a), caused by constructive interference of trapped modes within the sediment layer (Booth et al., 2014). We therefore set the higher corner frequency of our passband between 0.5 Hz and 1.0 Hz to maximize the SNR on each record and reduce the effect of the sediment reverberations. The low corner frequency of the passband is set to 0.1 Hz to filter out the long-period tilt and compliance noise (Crawford & Webb, 2000). After this QC procedure, 688 out of 2,002 records are identified for further receiver function analysis, with around 40 events at each station (Table 2). The signal to noise quality of the events can be seen in the average power spectra of all the events that pass quality check at the NoMelt stations used in this study (Figure 7a). A comprehensive description of the signal to noise at each station indicates that some stations have better signal to noise quality on average. We refer the reader to Figure S1 in Supporting information for the complete power spectra at each NoMelt station.

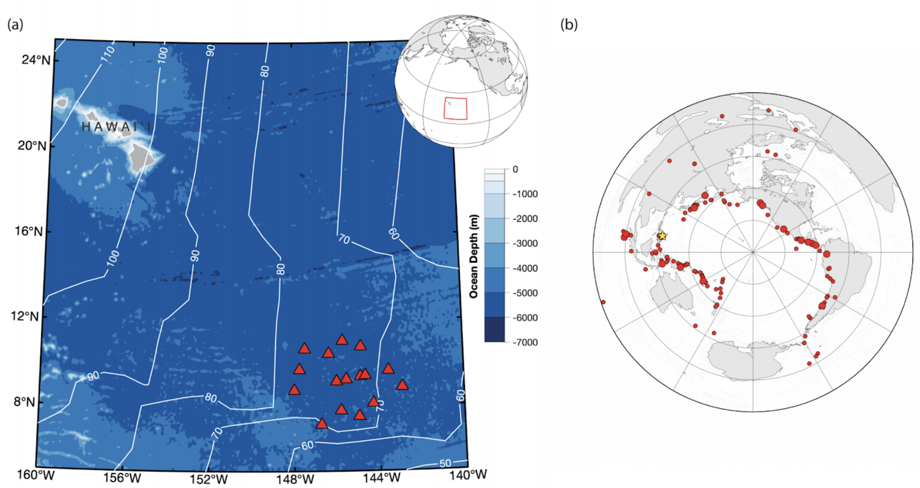

Figure 5. (a) Distribution of the OBS stations used in this study. The red triangles indicate the location of the stations. Detailed information (coordinates, elevation) can be found in Table 2. The color scale shows ocean depth; the white contour lines show the oceanic plate age in Ma (million years). The inset plot at the top right corner shows the location of the study area relative to the globe. (b) Azimuthal equidistant plot of all events used for RF analysis. Red circles indicate the location of the events; larger circles indicate events with magnitude larger than Mw7.0. The M7.6 event located at the eastern coast of the Philippines is marked as yellow pentagram, as its seismograms will be shown in Figure 6.

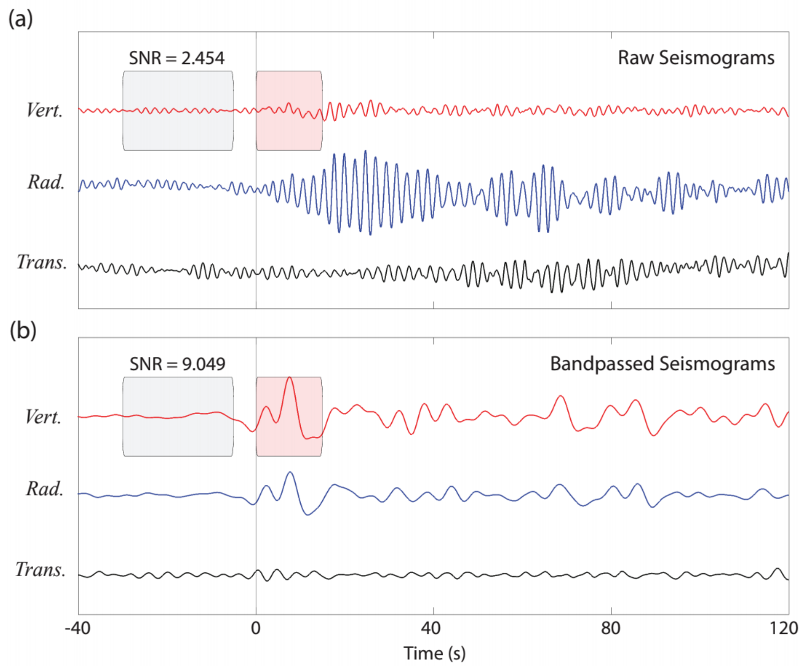

Figure 6. Seismograms of an M7.6 event recorded at station B13 showing the QC procedure. (a) raw seismograms; (b) bandpassed seismograms, both in Z-R-T coordinates. In the SNR calculation, signal and noise are defined as 0 - 15 s after and 20 - 5 s before the P arrival, respectively. The location of this event is marked in Figure 5a.

4.1 Earthquake & Noise Spectra: Signature of Sediment Resonance

We demonstrate the presence of sediment resonance on the NoMelt array by computing the multi-taper spectral estimates of the earthquake signals and pre-event noise. We observe sharp peaks on the earthquake signals that are absent on the noise spectra (Figure 7a). These peaks are also strongly coherent on the vertical and horizontal components at some stations, suggesting that they are signal-generated (Figure 7b). The amplitude and regularity of these peaks are strongest on the horizontal seismograms, confirming that they are sediment-induced resonances (Figure 1). The fundamental frequency is ~0.3Hz with the peaks becoming more pronounced at high frequencies (> 1Hz). While the average spectra across the network can be used to estimate the sediment properties, we point out that the individual resonance at each station is more complicated, with some stations showing stronger resonance than others, and the fundamental frequency of the sediment resonance varying from station to station (see Figure S1). This is the case for sediment properties that vary slightly across the network (i.e., thickness or shear velocity). Regardless, we use an average shear velocity and thickness of the sediment to design the dereverberation filter which approximates the average sediment structure across the array.

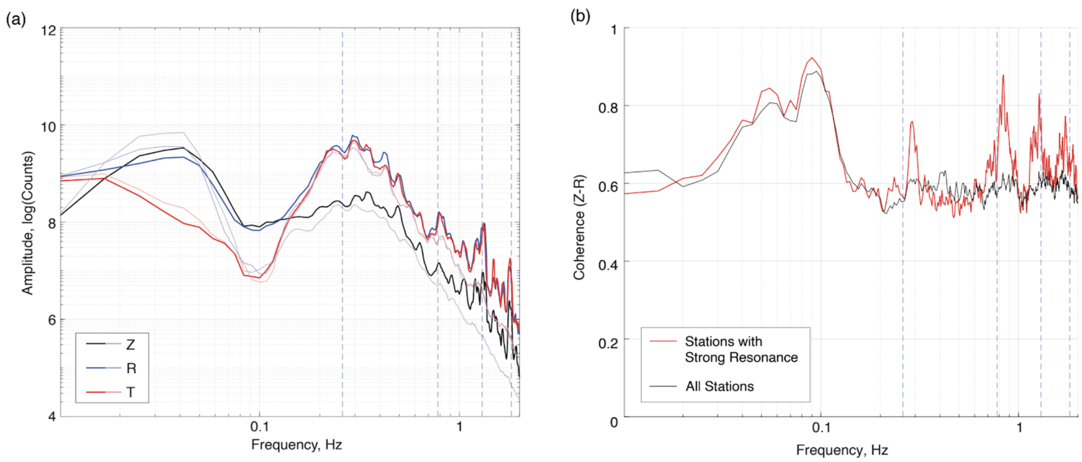

Figure 7. (a) Mean power spectra for all events at all stations used throughout the network. Black, blue and red lines indicate vertical, radial and transverse components, respectively; solid colors and lighter colors indicate P wave signal and pre-event noise, respectively. The spectra of P wave signal was calculated for a 120 s long time window starting 20 s before the P wave arrival; the spectra of pre-event noise was calculated for a 120 s long time window starting 180 s before the P wave arrival. Blue dashed vertical lines are sedimentary reverberation frequencies calculated from equation (14) based on a 250 m - thick sediment with shear velocity of 250 m/s. Detailed power spectra for each station can be found in Figure S1 in Supporting Information. (b) Mean coherence of vertical (Z) and radial (R) components for all events used at all stations (black line) and selected stations with strong resonance: B04, B08, B17 and B26 (red line). Blue dashed lines indicate the predicted sediment reverberations, same as in Figure 7a. Detailed coherence for each station can be found in Figure S2 in Supporting information.

4.2 Multi-Taper Receiver Function for Noisy Ocean Data

Although different types of deconvolution techniques have been advocated (Bostock, 2004; Rondenay, 2009), in this study, we choose to follow the approach of multi-taper spectral coherence technique (MTC-RFs) developed by (Park & Levin, 2000, 2016), which has shown promise for high-resolution imaging of crust and mantle structure in noisy environments like ocean islands (Leahy & Park, 2005; Olugboji & Park, 2015; Park & Rye, 2019) and the seafloor ocean bottom stations (Leahy et al., 2010; Olugboji, Park, Karato, et al., 2016).

The multi-taper spectral coherence approach improves frequency-dependent deconvolution in the following ways: (1) using tapers that are optimized for resistance to spectral leakage and, (2) discarding the incoherent portions of the wavefield by incorporating frequency-dependent variance-weighting for stacking receiver functions from multiple events. Frequency-domain MTC receiver functions are estimated using pre-event noise and the P-SV-SH tapered seismic records, $Y^k_{P,SV,SH}$, using k eigenspectra estimates:

$$R_{SV,SH}(f) = \frac{\sum_{k=0}^{K-1} Y_P^k(f) * Y_{SV,SH}^k(f)}{\sum_{k=0}^{K-1} Y_P^k(f) * Y_P^k(f) + S_o(f)} \qquad \textbf{(10)}$$

In real data, the pre-event noise spectrum, $S_o(f)$, and frequency-dependent variance, $\sigma_i^2(f)$ for each i seismic event is used to create a weighted average receiver function:

$$\bar{R}(f) = \frac{\sum_i^n w_i R_i(f)}{\sum_i^n w_i} \qquad \textbf{(11)}$$

the weighting function, $w_i = 1/\sigma_i^2(f)$, is computed using the coherence-derived variance:

$$\sigma_i^2 = \frac{1 - C_{P-SV}^2(f)}{(K-1)C_{P-SV}^2(f)} |R_i(f)|^2 \qquad \textbf{(12)}$$

and $C_{P-SV}^2(f)$ is the multi-taper coherence between P and SV records. For near-unity coherence, it is easy to see that the uncertainty is low (small variance) and for low coherence, the uncertainty is high (high variance). The last step in ensuring that the processed receiver functions are free from reverberations is the application of our dereverberation filter (equation (3)) in the frequency domain:

$$\widetilde{\bar{R}}(f) = \bar{R}(f) \cdot F(f) = \bar{R}(f)(1 + r_0 e^{-i2\pi f \Delta t}) \qquad \textbf{(13)}$$

We will discuss, in the following section, how to determine the filter parameters, r_0 and Δt, from the assumed velocity structures in the NoMelt region.

4.3 Application of a Dereverberation Filter to the NoMelt Data

We use the sediment properties of 250 m thickness inferred from the refraction model and a shear velocity of 250 m/s (Ruan et al., 2014; Russell et al., 2019). The value of sediment thickness fits well with global models on sediment structure (Straume et al., 2019). The P velocity of the water column is set to 1500 m/s; the P and S velocities of the crust is set to 6.5 km/s and 3.5 km/s, respectively; the P and S velocity of the uppermost mantle is set to 8.1 km/s and 4.5 km/s, respectively, according to previous studies (Lin et al., 2016; Mark et al., 2019; Russell et al., 2019; Tan & Helmberger, 2007). Similar to water reverberations, the sedimentary resonant frequencies can be calculated analytically:

$$f_n = \frac{(2n-1)v_s}{4H_s} \qquad \textbf{(14)}$$

where H_s and v_s are sediment thickness and shear velocity, respectively (Backus, 1959). We compare the resonant frequencies determined using the sediment properties with the power spectra obtained with multitaper spectral analysis (Figure 7a). The calculated resonant frequencies match the peaks on the signal power spectra, indicating that the sediment properties we choose can correctly describe the real reverberation effects. With these pre-assumed sediment and crustal structures, the filter parameters, $\Delta t =$ 2.0 s and $r_0 =$ 0.90, are then specified (see equation (5) and Text S1-A in Supporting Information).

We calculate the receiver functions with a cutoff frequency of 1.5 Hz for all 16 stations, using the multi-taper spectral coherence approach described above. We then stack all the receiver function traces across the network to get a better coverage of epicentral distances (Figure 8a). The first P arrival is clear in raw RFs, but all Moho and LAB conversions, and their multiples, are hardly visible due to severe reverberations. We apply the proposed dereverberation filter to get filtered RFs (Figure 8b). After filtering, the first Ps conversion from the Moho (*PmS*) is clearly visible at ~2 s; the first Moho multiple (*PPmS*), though not as clear as *PmS* phase, is also visible at ~4.5 s; *PSmS* phase is still not visible, which is expected due to its low amplitude (Table 2). The first Ps conversion from the seismic LAB is very clear at ~9 s, with the expected positive moveout, especially at higher epicentral distances, which is promising in determining the LAB depth. We then implement the 1-D search for Moho and seismic LAB depth to the raw and filtered RFs, given fixed ocean mantle velocity structures from previous studies (Mark et al., 2019; Russell et al., 2019; Tan & Helmberger, 2007) (Table 1).

Since there are no clear positive peaks at the predicted *PmS* arrival time in the raw RF traces, the H search for Moho using raw RFs fails, with a wrongly identified crustal thickness of 5.0 km, which is at the boundary of the search interval (Figure 8c). A search for the seismic LAB gives a depth of 71 km; however, due to ambiguous peaks around the predicted *PlS* phase in the RF traces, the line-search shows multiple peaks (e.g., at ~59 km and ~66 km in Moho-LAB thickness in Figure 8d), making it difficult to interpret. The results using filtered RF traces gives more reliable results. Using appropriate weighting for different phases(Table 2), we recover a crustal thickness of 8.6±0.6 km (Figure 8e). Since the *PlS* phase is clearly visible with correct moveout after applying the dereverberation filter, the results for the seismic LAB shows an unambiguous major peak at the Moho-LAB thickness of 64 km, giving an LAB depth of 72±1 km (Figure 8f).

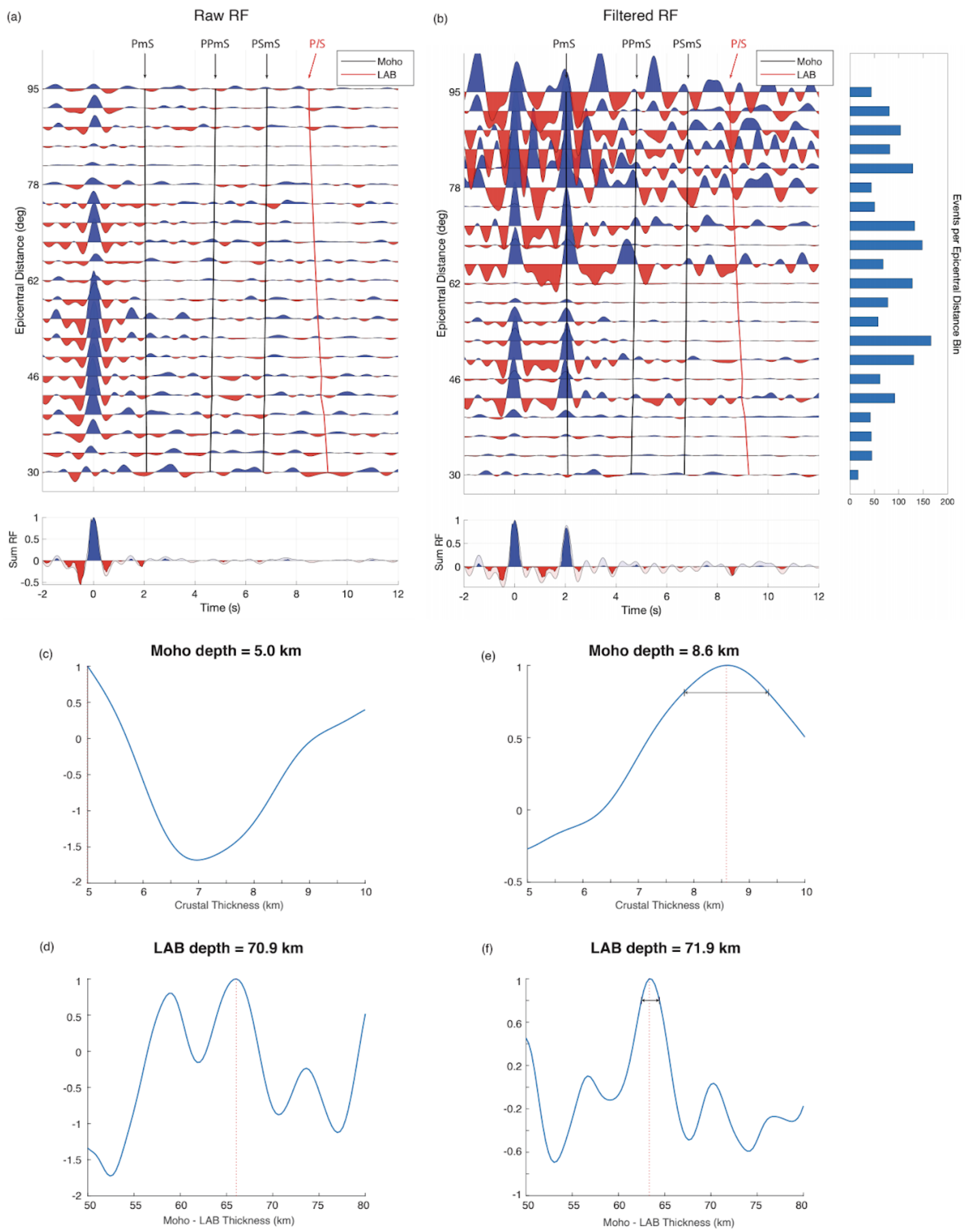

Figure 8. Receiver function traces and linear search for Moho and LAB depth using OBS data from NoMelt experiment. (a) Raw RF traces plotted against epicentral distance. The predicted arrival times for direct Ps conversions and multiples from the Moho are marked as green solid, dashed and dotted lines, respectively; Ps conversion from the LAB is marked as black solid line. (b) Filtered RF traces plotted against epicentral distance. The predicted travel times for different phases are marked the same as Figure 8a. Number of events used in each epicentral distance bin is shown in the histogram on the right. (c) Linear search for the depth of Moho given fixed crustal κ and v_p, using raw RF shown in Figure 8a. (d) Linear search for the Moho - LAB thickness given fixed crustal and mantle κ and v_p, using raw RF shown in Figure 8a. (e) Linear search for the depth of Moho given fixed crustal κ and v_p, using filtered RF shown in Figure 8b. (f) Linear search for the Moho - LAB thickness given fixed crustal and mantle κ and v_p, using filtered RF shown in Figure 8b.

4.4 Filter Sensitivity & Robustness

We note that the filter is mostly sensitive to the two-way travel time and only weakly sensitive to the reverberation strength. We show how the uncertainties in the knowledge of the sediment properties may affect the effectiveness of a slightly inaccurate dereverberation filter. For a range of sediment thicknesses and shear velocities with an unknown sediment reverberation effect, an approximate filter will still perform reliably well. The effectiveness of such a filter is quantified by a 'robustness' factor that describes how well it matches the reverberation effect of a sediment layer:

$$\gamma = \left| \int_0^{1.5Hz} E(H_i, v_j, f) \right| \cdot \left| \int_0^{1.5Hz} F(H_{ref}, v_{ref}, f) \right| \tag{15}$$

where $E(H_i, v_j, f)$ is the reverberation effect in the frequency domain, generated using sediment thickness H_i and shear velocity v_j; $F(H_{ref}, v_{ref}, f)$ is the filter in the frequency domain generated using the reference sediment properties (H_{ref} = 250 m and v_{ref} = 250 m/s). The mismatch between the filter and reverberations are evaluated to 1.5 Hz, which is the nominal cutoff frequency at which our NoMelt receiver functions are calculated. Note that $\gamma = 1$ if $H_i = H_{ref}$ and $v_j = v_{ref}$, which is the case when the filter and the sediment properties are properly matched (equation (3c)).

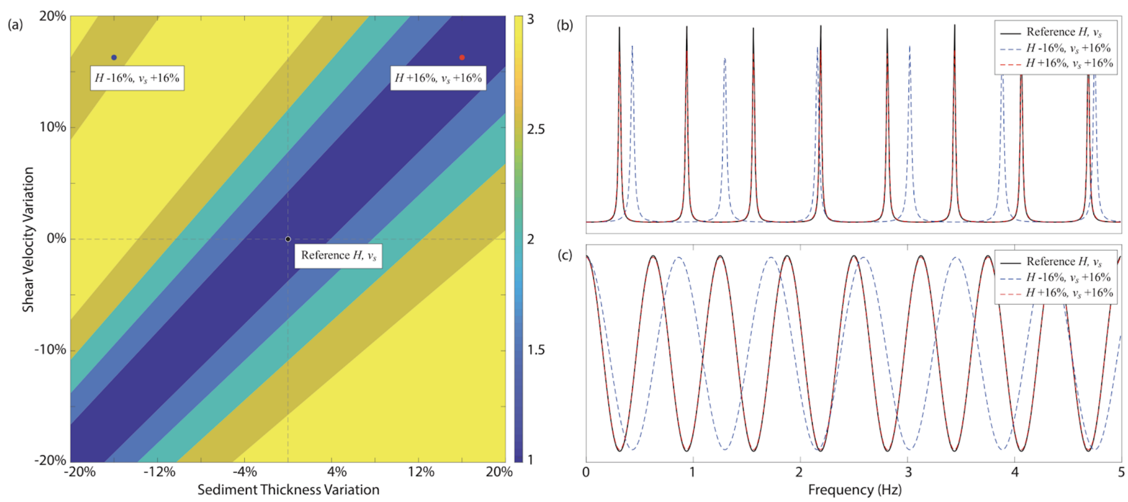

Figure 9. Robustness of the dereverberation filter depending on the sediment properties. (a) The horizontal and vertical axes indicate variations in sediment thickness and shear velocity, respectively, both ranging from -20% to +20% compared to the reference sediment thickness and shear velocity: 250 m and 250 m/s. The color from blue to yellow refers to the robustness factor ranging from 1 to 3, indicating that the effectiveness of the reference filter on the specific sediment is lesser than that on the reference sediment. The black dot is the reference sediment thickness and shear velocity; the blue and red dots are two pairs of sediment properties. The resonance and filter generated from these sediments are shown in Figure 9b and Figure 9c. (b) Resonance of the sediment in the frequency domain. Black line: reference sediment; blue dashed line: -16% in thickness and +16% in shear

velocity compare to the reference sediment (blue dot in Figure 9a); red dashed line: +16% in thickness and +16% in shear velocity compare to the reference sediment (red dot in Figure 9a). (c) Corresponding filters of the resonances shown in Figure 9b.

The reference filter remains effective if the delay time of the filter matches that of the sediment, and can happen when the thickness and shear velocity both increase or decrease by roughly the same amount (along the bottom left - top right diagonal in Figure 9a). For example, if the sediment thickness and shear velocity both increase by 16%, the reverberations and the corresponding filters are highly alike; however, a 16% decrease in thickness and 16% increase in shear velocity could result in significant degradation of the effectiveness of the reference filter (Figure 9b-c). This indicates that the filter is mostly sensitive to the two-way travel time (equation (5)), which is proportional to the ratio of sediment thickness and shear velocity. This property means that only the ratio needs be constrained during filter design, and as we have demonstrated, may be verified using data spectra (Figure 7 and equation (14)).

5.0 A Sharp Velocity Reduction: 'Seismic' LAB of a Normal Ocean

The strength and sharpness of the LAB, in terms of both velocity and depth gradient, can be inferred from the width and amplitude of the pulse associated with the Ps conversion from the LAB (i.e. *PlS* phase) in the receiver functions. *PlS* phase is clearly observed at higher epicentral distance bins after applying the dereverberation filter (Figure 9b); the average width of the negative pulse of *PlS* phase is ~0.5 s. For receiver functions calculated at 1.5 Hz, a 0.5 s pulse width implies a relatively sharp transition in depth of no more than 5 km (Olugboji et al., 2013).

The percent velocity drop at the LAB can be predicted from the relative amplitude ratio of the *PmS* and *PlS* phases in the RF traces. We generate synthetic receiver functions using different shear velocity drops at the LAB interface (while keeping other velocities fixed), and calculate the amplitude ratios between *PlS* and *PmS* phases at higher epicentral distances. The *PlS*/*PmS* amplitude ratio depends on the velocity contrast across the LAB, following a roughly linear trend. A stronger velocity contrast leads to a larger amplitude for the Ps conversion from the LAB (Figure 10). We place constraints on the *PlS*/*PmS* amplitude ratio, (0.37 ± 0.13), based on the *PmS* and *PlS* phases clearly visible at ~ 2s and 9s on the RF traces (Figure 9b). We then infer the amplitude ratio $\Delta v_s/v_s$ from our synthetic modeling, suggesting a shear velocity reduction of ~6.8 ± 2.6 % at the LAB in the *NoMelt* region.

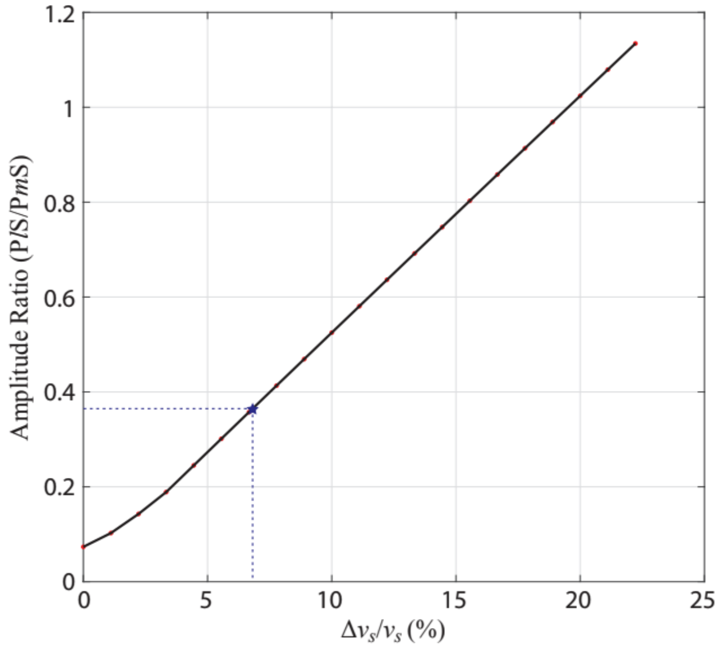

Figure 10. Determination of strength of velocity drop at the LAB from synthetic receiver functions. $\Delta v_s/v_s$ on the horizontal axis is the percentage of shear velocity drop from lithosphere to asthenosphere at the LAB. The vertical axis is the average amplitude ratio of *PlS* and *PmS* phases calculated at higher epicentral distances. The blue star indicates the predicted LAB velocity gradient at the NoMelt region from the measured amplitude ratio from filtered RF traces.

6.0 Discussion

Complementary magnetotelluric studies across the NoMelt array have shown that the lithosphere is resistive to a depth of ~80 km (Sarafian et al., 2015), and the transition to a conductive asthenosphere can be explained exclusively by dehydration during ocean crust formation. Surface wave attenuation measurements across the array show a transition from a low to high attenuation layer at ~ 70 km, which coincides with a transition to a low velocity layer (Ma et al., 2020). A joint assessment of the conductivity and attenuation, together with our new results on the depth (72 km) and gradient sharpness (<5 km) of the seismic LAB structure, agrees closely with the predictions of the elastically accommodated grain-boundary sliding (EAGBS) model presented by (Karato & Park, 2018; Olugboji et al., 2013). This is broadly consistent with earlier receiver function tests from older (145 Ma) Pacific lithosphere (Olugboji, Park, Karato, et al., 2016). Our new receiver function results are broadly consistent with results from the mid-atlantic oceanic lithosphere of similar age (K. Hannemann et al., 2017), although we note that none of the past RF studies address the issue of removing sediment reverberations from ocean bottom seismic data. In the Pacific, a comparison with other body-wave techniques not affected by reverberations (e.g., SS precursors), indicates that our inferred seismic LAB depth is broadly consistent with early results (Gaherty et al., 1996; Ma et al., 2020; Tan & Helmberger, 2007) (see summary in

Figure 11). Although the SS precursor technique seems to show an age dependence for normal Pacific lithosphere (C. Rychert et al., 2020; C. A. Rychert et al., 2018b), the very high resolution of our receiver function results (~1.5 Hz) allows us to improve on the resolution of the inferred depth and sharpness of the seismic LAB.

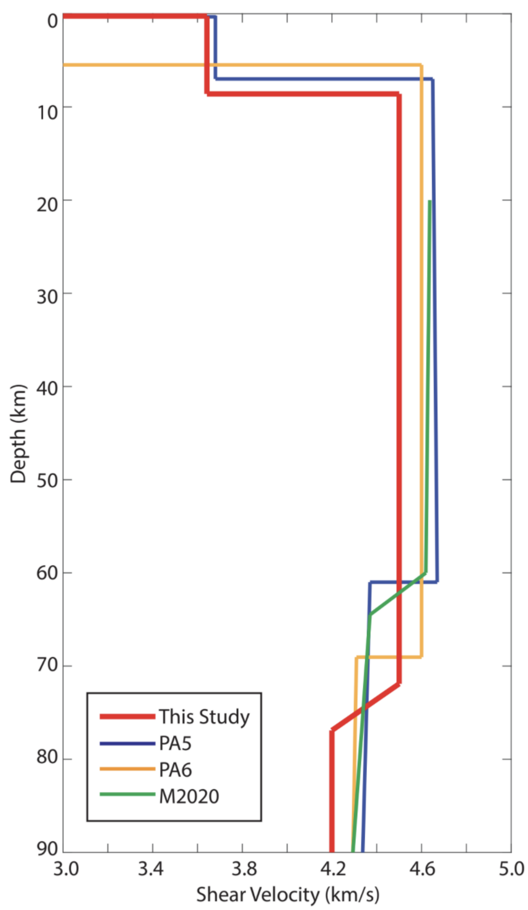

Figure 11. Comparison of shear velocity profiles obtained in this study and some other models: PA5 (Gaherty et al., 1996), PA6 (Tan & Helmberger, 2007), and M2020 (Ma et al., 2020).

Our approach of filtering out the sediment reverberations makes inference on subsurface structure more robust. Other proposed techniques, e.g., using band-limited receiver functions (K. Hannemann et al., 2017), or a transfer-function approach that does away with deconvolution (Akuhara et al., 2019; Audet, 2016; Thomas Bodin et al., 2014; Frederiksen & Delaney, 2015) may either be inadequate for high resolution imaging or may retain complexities that complicate the interpretation of subsurface structures, in the case of a highly reverberatory sediment layer. A band-limited receiver function approach attenuates sharp-discontinuities and masks thinly layered structures, while a transfer function approach requires a-priori constraints on the elastic properties of the sediment layer. In both cases, if the wavelength of the trapped waves in the sediment layer is similar to that of the subsurface structure it will strongly imprint on the green's function and may result in difficulty of recovering a clear image of subsurface structure (e.g., crust and mantle layering). We therefore recommend an approach of tuned dereverberation filtering whenever possible, especially when the signature of a sediment or shallow water reverberation is strongly observed in the data spectra (e.g., Figure 7a). Even when sediment properties are not completely prescribed, an appropriate filter can still be designed from empirical estimates of the two-way travel time, which can be validated from the spectra or coherence measurements.

7.0 Conclusions

We show that, with an appropriate filter, stable high-resolution receiver function imaging of the lithosphere can be obtained from sea-floor stations and can therefore be used to complement long-wavelength surface wave studies for testing models of oceanic plate origin and evolution (T. Bodin et al., 2012; Gao & Lekić, 2018). We used multi-taper spectral analysis to improve the detection of earthquake signals buried in noisy data and to validate the parameters of our filter. We confirm that the expected resonance frequencies for the sedimentary layer matches the spectra and coherence pattern of seismic data. The application of a dereverberation filter to the receiver functions will be useful for a growing fleet of ocean bottom deployments (Kawakatsu & Utada, 2017; C. A. Rychert et al., 2018b; Takeo et al., 2018) and can advance our understanding of the origin and nature of the seismic lithosphere asthenosphere boundary in the oceanic plates. In application to newly collected marine seismic data (Barcheck et al., 2020; Kohler et al., 2020), we anticipate that post-processing the receiver functions using the recommended dereverberation filter will improve scattered wave imaging, especially with amphibious seismic arrays where the water and sediment layer is expected to vary significantly (Barcheck et al., 2020; A. K. Doran & Laske, 2019; Janiszewski & Abers, 2015; Lynner et al., 2020).

8.0 Acknowledgments

This work was made possible by grants and support from the National Science Foundation under grant number: 1818654. The authors acknowledge the use of the BlueHive Linux cluster at the University of Rochester's center for integrated research computing - CIRC (https://www.circ.rochester.edu/). All seismic data used in this study can be obtained from the IRIS Data management center (https://ds.iris.edu/ds) under network code ZA. Horizontal orientations for individual stations are reported in (Russell et al., 2019) and estimated using the DLOPy (Adrian K. Doran & Laske, 2017) code available on github. Multi-taper spectral analysis was conducted using the MATLAB jlab library provided by (Lilly, 2017). Synthetic receiver functions were computed using the telewaveism open-source python library provided by (Audet et al., 2019). Reflection and transmission coefficients for a two-layer model was simulated using the MATLAB code of Charles Ammon. The Receiver function deconvolution was computed using compiled C++ code provided by (Olugboji & Park, 2016). The binary source, Earthquake metadata, and processed receiver function SAC traces can be retrieved from (Zhang & Olugboji, 2020). We acknowledge many helpful discussions with Baowei Liu, Jeffrey Park, and Shun-ichiro Karato.

9.0 References Cited

Aki, K., & Richards, P. G. (2002). *Quantitative Seismology, 2nd Ed.*

Akuhara, T., & Mochizuki, K. (2015). Hydrous state of the subducting Philippine Sea plate inferred from receiver function image using onshore and offshore data. *Journal of Geophysical Research, [Solid Earth]*, *120*(12), 8461–8477.

Akuhara, T., Mochizuki, K., Kawakatsu, H., & Takeuchi, N. (2016). Non-linear waveform analysis for water-layer response and its application to high-frequency receiver function analysis using OBS array. *Geophysical Journal International*, *206*(3), 1914–1920.

Akuhara, T., Mochizuki, K., Kawakatsu, H., & Takeuchi, N. (2017). A fluid-rich layer along the Nankai trough megathrust fault off the Kii Peninsula inferred from receiver function inversion. *Journal of Geophysical Research, [Solid Earth]*, *122*(8), 6524–6537.

Akuhara, T., Bostock, M. G., Plourde, A. P., & Shinohara, M. (2019). Beyond Receiver Functions: Green's Function Estimation by Transdimensional Inversion and Its Application to OBS Data. *Journal of Geophysical Research, [Solid Earth]*, *124*(2), 1944–1961.

Audet, P. (2016). Receiver functions using OBS data: promises and limitations from numerical modelling and examples from the Cascadia Initiative. *Geophysical Journal International*, *205*(3), 1740–1755.

Audet, P., Thomson, C. J., Bostock, M. G., & Eulenfeld, T. (2019). Telewavesim: Python software for teleseismic body wave modeling. *Journal of Open Source Software*, *4*(44), 1818.

Backus, M. M. (1959). WATER REVERBERATIONS—THEIR NATURE AND ELIMINATION. *Geophysics*, *24*(2), 233–261.

Barcheck, G., Abers, G. A., Adams, A. N., Bécel, A., Collins, J., Gaherty, J. B., et al. (2020). The Alaska Amphibious Community Seismic Experiment. *Seismological Research Letters*, *91*(6), 3054–3063.

Bodin, T., Sambridge, M., Tkalčić, H., Arroucau, P., Gallagher, K., & Rawlinson, N. (2012). Transdimensional inversion of receiver functions and surface wave dispersion. *Journal of Geophysical Research, [Solid Earth]*, *117*(B2). https://doi.org/10.1029/2011JB008560

Bodin, T., Yuan, H., & Romanowicz, B. (2014). Inversion of receiver functions without deconvolution—application to the Indian craton. *Geophysical Journal International*, *196*(2), 1025–1033.

Booth, C. M., Forsyth, D. W., & Weeraratne, D. S. (2014). Upper mantle Q structure beneath old seafloor in the western Pacific. *Journal of Geophysical Research, [Solid Earth]*, *119*(4), 3448–3461.

Bostock, M. G. (2004). Theory and Observations -Teleseismic Body-Wave Scattering and Receiver-Side Structure. *Treatise in Geophysics*, 235–246.

Bostock, M. G., & Kumar, M. R. (2010). Bias in seismic estimates of crustal properties. *Geophysical Journal International*. Retrieved from https://academic.oup.com/gji/article-abstract/182/1/403/563322

Bostock, M. G., & Trehu, A. M. (2012). Wave-field decomposition of ocean bottom seismograms. *Bulletin of the Seismological Society of America*, *102*(4), 1681–1692.

Crawford, W. C., & Webb, S. C. (2000). Identifying and removing tilt noise from low-frequency (< 0.1 Hz) seafloor vertical seismic data. *Bulletin of the Seismological Society of America*, *90*(4), 952–963.

Cunningham, E., & Lekic, V. (2019). Constraining crustal structure in the presence of sediment: a multiple converted wave approach. *Geophysical Journal International*, *219*(1), 313–327.

Doran, A. K., & Laske, G. (2017). Ocean−Bottom Seismometer Instrument Orientations via Automated Rayleigh−Wave Arrival−Angle MeasurementsOcean−Bottom Seismometer Instrument Orientations via Automated Rayleigh−Wave Arrival−Angle Measurements. *Bulletin of the Seismological Society of America*, *107*(2), 691–708.

Doran, A. K., & Laske, G. (2019). Seismic Structure of Marine Sediments and Upper Oceanic Crust Surrounding Hawaii. *Journal of Geophysical Research, [Solid Earth]*, *124*(2), 2038–2056.

Dziewonski, A. M., & Anderson, D. L. (1981). Preliminary reference Earth model. *Physics of the Earth and Planetary Interiors*, *25*(4), 297–356.

Eaton, D. W., Darbyshire, F., Evans, R. L., Grütter, H., Jones, A. G., & Yuan, X. (2009). The elusive lithosphere–asthenosphere boundary (LAB) beneath cratons. *Lithos*, *109*(1-2), 1–22.

Frederiksen, A. W., & Delaney, C. (2015). Deriving crustal properties from the P Coda without deconvolution: the southwestern Superior Province, North America. *Geophysical Journal International*, *201*(3), 1491–1506.

Gaherty, J. B., Jordan, T. H., & Gee, L. S. (1996). Seismic structure of the upper mantle in a central Pacific corridor. *Journal of Geophysical Research*, *101*(B10), 22291.

Gao, C., & Lekić, V. (2018). Consequences of parametrization choices in surface wave inversion: insights from transdimensional Bayesian methods. *Geophysical Journal International*, *215*(2), 1037–1063.

Godin, O. A., & Chapman, D. M. F. (1999). Shear-speed gradients and ocean seismo-acoustic noise resonances. *The Journal of the Acoustical Society of America*, *106*(5), 2367.

Hannemann, K., Krüger, F., Dahm, T., & Lange, D. (2016). Oceanic lithospheric S-wave velocities from the analysis of P-wave polarization at the ocean floor. *Geophysical Journal International*, *207*(3), 1796–1817.

Hannemann, K., Krüger, F., & Dahm, T. (2017). Structure of the oceanic lithosphere and upper mantle north of the Gloria fault in the eastern mid−Atlantic by receiver function analysis. *Journal of Geophysical Research*. Retrieved from https://agupubs.onlinelibrary.wiley.com/doi/abs/10.1002/2016JB013582

Helffrich, G., & Thompson, D. (2010). A stacking approach to estimate VP/VS from receiver functions: Stacking to estimate VP/VS. *Geophysical Journal International*, *182*(2), 899–902.

Hirschmann, M. M. (2010). Partial melt in the oceanic low velocity zone. *Physics of the Earth and Planetary Interiors*, *179*(1-2), 60–71.

Janiszewski, H. A., & Abers, G. A. (2015). Imaging the Plate Interface in the Cascadia Seismogenic Zone: New Constraints from Offshore Receiver Functions. *Seismological Research Letters*, *86*(5), 1261–1269.

Karato, S.-I. (2012). On the origin of the asthenosphere. *Earth and Planetary Science Letters*, *321-322*, 95–103.

Karato, S.-I., & Park, J. (2018). On the Origin of the Upper Mantle Seismic Discontinuities. *Lithospheric Discontinuities*, 5–34.

Kawakatsu, H., & Abe, Y. (2016). Significance of sediment reverberations on receiver functions of broadband OBS data: Comments on

Olugboji et al. (2016) “Nature of the Seismic Lithosphere-Asthenosphere Boundary within Normal Oceanic Mantle from High-Resolution Receiver Functions.” *Geochemistry, Geophysics, Geosystems*. https://doi.org/10.1002/2016GC006418

Kawakatsu, H., & Utada, H. (2017). Seismic and Electrical Signatures of the Lithosphere – Asthenosphere System of the Normal Oceanic. https://doi.org/10.1146/annurev-earth-063016-020319

Kawakatsu, H., Kumar, P., Takei, Y., Shinohara, M., Kanazawa, T., Araki, E., & Suyehiro, K. (2009). Seismic evidence for sharp lithosphere-asthenosphere boundaries of oceanic plates. *Science* , *324*(5926), 499–502.

Kennett, B. L. N., Engdahl, E. R., & Buland, R. (1995). Constraints on seismic velocities in the Earth from traveltimes. *Geophysical Journal International*, *122*(1), 108–124.

Kohler, M. D., Hafner, K., Park, J., Irving, J. C. E., Caplan−Auerbach, J., Collins, J., et al. (2020). A Plan for a Long−Term, Automated, Broadband Seismic Monitoring Network on the Global Seafloor. *Seismological Research Letters*, *91*(3), 1343–1355.

Kumar, M. R., & Bostock, M. G. (2008). Extraction of absolute P velocity from receiver functions. *Geophysical Journal International*, *175*(2), 515–519.

Kumar, P., Kawakatsu, H., Shinohara, M., Kanazawa, T., Araki, E., & Suyehiro, K. (2011). P and S receiver function analysis of seafloor borehole broadband seismic data. *Journal of Geophysical Research*, *116*(B12), B12308.

Leahy, G. M., & Park, J. (2005). Hunting for oceanic island Moho. *Geophysical Journal International*, *160*(3), 1020–1026.

Leahy, G. M., Collins, J. A., Wolfe, C. J., Laske, G., & Solomon, S. C. (2010). Underplating of the Hawaiian Swell: evidence from teleseismic receiver functions. *Geophysical Journal International*, *183*(1), 313–329.

Lilly, J. M. (2017). jLab: A data analysis package for Matlab, v. 1.6. 5. *See Http://www. Jmlilly. Net/jmlsoft. Html*.

Lin, P.-Y. P., Gaherty, J. B., Jin, G., Collins, J. A., Lizarralde, D., Evans, R. L., & Hirth, G. (2016). High-resolution seismic constraints on flow dynamics in the oceanic asthenosphere. *Nature*, *535*(7613), 538–541.

Liu, Y., Liu, B., Liu, C., & Hua, Q. (2020). The crustal structure of the Eastern Subbasin of the South China Sea: constraints from receiver functions. *Geophysical Journal International*, *222*(2), 1003–1012.

Lynner, C., JA Van Avendonk, H., Bécel, A., Christeson, G. L., Dugan, B., Gaherty, J. B., et al. (2020). The Eastern North American Margin Community Seismic Experiment: An Amphibious Active-and Passive-Source Dataset. *Seismological Research Letters*, *91*(1), 533–540.

Mark, H. F., Lizarralde, D., & Collins, J. A. (2019). Azimuthal seismic anisotropy of 70−Ma Pacific−plate upper mantle. *Journal of*. Retrieved from https://agupubs.onlinelibrary.wiley.com/doi/abs/10.1029/2018JB016451

Ma, Z., Dalton, C. A., Russell, J. B., Gaherty, J. B., Hirth, G., & Forsyth, D. W. (2020). Shear attenuation and anelastic mechanisms in the central Pacific upper mantle. *Earth and Planetary Science Letters*, *536*, 116148.

Olugboji, T. M., & Park, J. (2015). Crustal Anisotropy beneath selected Pacific-Ocean Islands from Harmonic Decomposition of Recevier Functions. *In Revision, Geochemistry Geophysics Geosystems*.

Olugboji, T. M., & Park, J. (2016). Crustal anisotropy beneath Pacific Ocean-Islands from harmonic decomposition of receiver functions. *Geochemistry, Geophysics, Geosystems*, *17*(3), 810–832.

Olugboji, T. M., Karato, S.-I., & Park, J. (2013). Structures of the oceanic lithosphere-asthenosphere boundary: Mineral-physics modeling and seismological signatures. *Geochemistry, Geophysics, Geosystems*, *14*(4), 880–901.

Olugboji, T. M., Park, J., Karato, S.-I., & Shinohara, M. (2016). Nature of the seismic lithosphere-asthenosphere boundary within normal oceanic mantle from high-resolution receiver functions. *Geochemistry, Geophysics, Geosystems*, *17*(4), 1265–1282.

Olugboji, T. M., Park, J., & Karato, S.-I. (2016). Reply to comment by Kawakatsu and Abe on “Nature of the seismic lithosphere-asthenosphere boundary within normal oceanic mantle from high-resolution receiver functions.” *Geochemistry, Geophysics, Geosystems*, *17*(8), 3493–3501.

Osen, A., Amundsen, L., & Reitan, A. (1999). Removal of water-layer multiples from multicomponent sea-bottom data. *Geophysics*, *64*(3), 838–851.

Park, J., & Levin, V. (2000). Receiver Functions from Multiple-Taper Spectral Correlation Estimates. *Bulletin of the Seismological Society of America*, *90*(6), 1507–1520.

Park, J., & Levin, V. (2016). Statistics and frequency-domain moveout for multiple-taper receiver functions. *Geophysical Journal International*, *207*(1), 512–527.

Park, J., & Rye, D. M. (2019). Why Is Crustal Underplating Beneath Many Hot Spot Islands Anisotropic? *Geochemistry, Geophysics, Geosystems*, *20*(11), 4779–4809.

Rondenay, S. (2009). Upper Mantle Imaging with Array Recordings of Converted and Scattered Teleseismic Waves. *Surveys in Geophysics*, *30*(4), 377–405.

Ruan, Y., Forsyth, D. W., & Bell, S. W. (2014). Marine sediment shear velocity structure from the ratio of displacement to pressure of Rayleigh waves at seafloor. *Journal of Geophysical Research, [Solid Earth]*, *119*(8), 6357–6371.

Russell, J. B., Gaherty, J. B., Lin, P. P., Lizarralde, D., Collins, J. A., Hirth, G., & Evans, R. L. (2019). High−Resolution Constraints on Pacific Upper Mantle Petrofabric Inferred From Surface−Wave Anisotropy. *Journal of Geophysical Research, [Solid Earth]*, *124*(1), 631–657.

Rychert, C., Harmon, N., Constable, S., & Wang, S. (2020). The nature of the Lithosphere−Asthenosphere Boundary. *Journal of Geophysical Research, [Solid Earth]*. https://doi.org/10.1029/2018JB016463

Rychert, C. a., Laske, G., Harmon, N., & Shearer, P. M. (2013). Seismic imaging of melt in a displaced Hawaiian plume. *Nature Geoscience*, *6*(8), 657–660.

Rychert, C. A., Harmon, N., & Tharimena, S. (2018a). Scattered wave imaging of the oceanic plate in Cascadia. *Science Advances*, *4*(2), eaao1908.

Rychert, C. A., Harmon, N., & Tharimena, S. (2018b). Seismic Imaging of the base of the ocean plates. *Lithospheric Discontinuities*, *239*, 71.

Sarafian, E., Evans, R. L., Collins, J. a., Elsenbeck, J., Gaetani, G. a., Gaherty, J. B., et al. (2015). The electrical structure of the central Pacific upper mantle constrained by the NoMelt experiment. *Geochemistry, Geophysics, Geosystems*, *16*(4), 1115–1132.

Snieder, R., & Snieder, R. A. (2001). *A Guided Tour of Mathematical Methods: For the Physical Sciences*. Cambridge University Press.

Straume, E. O., Gaina, C., Medvedev, S., Hochmuth, K., Gohl, K., Whittaker, J. M., et al. (2019). GlobSed: Updated Total Sediment Thickness in the World’s Oceans. *Geochemistry, Geophysics, Geosystems*, *20*(4), 1756–1772.

Takeo, A., Kawakatsu, H., Isse, T., & Nishida, K. (2018). In Situ Characterization of the Lithosphere−Asthenosphere System beneath NW

Pacific Ocean Via Broadband Dispersion Survey With Two OBS Arrays. *Geochemistry: Exploration, Environment, Analysis*. Retrieved from https://agupubs.onlinelibrary.wiley.com/doi/abs/10.1029/2018GC007588

Tan, Y., & Helmberger, D. V. (2007). Trans-Pacific upper mantle shear velocity structure. *Journal of Geophysical Research, [Solid Earth]*, *112*(B8). Retrieved from https://agupubs.onlinelibrary.wiley.com/doi/abs/10.1029/2006JB004853

Thorwart, M., & Dahm, T. (2005). Wavefield decomposition for passive ocean bottom seismological data. *Geophysical Journal International*, *163*(2), 611–621.

Yeck, W. L., Sheehan, A. F., & Schulte-Pelkum, V. (2013). Sequential H- Stacking to Obtain Accurate Crustal Thicknesses beneath Sedimentary Basins. *Bulletin of the Seismological Society of America*. https://doi.org/10.1785/0120120290

Yu, Y., Song, J., Liu, K. H., & Gao, S. S. (2015). Determining crustal structure beneath seismic stations overlying a low-velocity sedimentary layer using receiver functions. *Journal of Geophysical Research, [Solid Earth]*, *120*(5), 3208–3218.

Zhang, Z., & Olugboji, T. (2020). *URseismology/RFDereverb: V1.0*. https://doi.org/10.5281/zenodo.4359598

Zhu, L., & Kanamori, H. (2000). Moho depth variation in southern California from teleseismic receiver functions. *Journal of Geophysical Research*, *105*(B2), 2969–2980.

JGR, Solid Earth

Supporting Information for

The Signature and Elimination of Sediment Reverberations on Submarine Receiver Functions

Ziqi Zhang[1*], and Tolulope Olugboji[1]

[1] *Department of Earth and Environmental Sciences, University of Rochester, NY*

Contents of this file

Text S1, S2; Figures S1, S2; Table S1.

Introduction

We provide supporting information showing extended analysis: Text S1 shows how we derive the amplitudes and polarities of different phases in the receiver functions using reflection and transmission coefficients; Text S2 shows how we adjust the traveltimes in the $\kappa - v_p - H$ stacks when sediment presents; Figure S1 and Figure S2 show the mean power spectra and coherence on vertical and radial components at each station, respectively; Table S1 shows detailed information of each station.

Text S1

Text S1-A: Reflection and Transmission Coefficient Matrices

Seismic reflection and transmission coefficients depend on the seismic wave velocities and densities on either side of the boundary and on the incident wave horizontal slowness, or ray parameter. The coefficients are given by (Aki and Richards 2002; Lay and Wallace 1995):

$$R_{pp} = [(b\eta_{\alpha_1} - c\eta_{\alpha_2})F - (a + d\eta_{\alpha_1}\eta_{\beta_2})Hp^2]/D$$

$$R_{ps} = -2[\eta_{\alpha_1}(ab + cd\eta_{\alpha_2}\eta_{\beta_2})p(\alpha_1/\beta_1)]/D$$

$$R_{ss} = -[(b\eta_{\beta_1} - c\eta_{\beta_2})E - (a + b\eta_{\alpha_2}\eta_{\beta_1})Gp^2]/D$$

$$R_{sp} = -[2\eta_{\beta_1}(ab + cd\eta_{\alpha_2}\eta_{\beta_2})p(\beta_1/\alpha_1)]/D$$

$$T_{pp} = [2\rho_1\eta_{\alpha_1}F(\alpha_1/\alpha_2)]/D$$

$$T_{ps} = [2\rho_1\eta_{\alpha_1}Hp(\alpha_1/\beta_2)]/D$$

$$T_{ss} = [2\rho_1\eta_{\beta_1}E(\alpha_2/\beta_2)]/D$$

$$T_{sp} = -[2\rho_1\eta_{\beta_1}Gp(\alpha_2/\beta_1)]/D$$

where

$$a = \rho_2(1 - 2\beta_2^2p^2) - \rho_1(1 - 2\beta_1^2p^2)$$

$$b = \rho_2(1 - 2\beta_2^2p^2) + 2\rho_1\beta_1^2p^2$$

$$c = \rho_1(1 - 2\beta_1^2p^2) + 2\rho_2\beta_2^2p^2$$

$$d = 2(\rho_2\beta_2^2 - \rho_1\beta_1^2)$$

$$E = b\eta_{\alpha_1} + c\eta_{\alpha_2}$$

$$F = b\eta_{\beta_1} + c\eta_{\beta_2}$$

$$G = a - d\eta_{\alpha_1}\eta_{\beta_2}$$

$$H = a - d\eta_{\alpha_2}\eta_{\beta_1}$$

$$D = EF + GHp^2$$

Text S1-B: Amplitude and Polarity of Phases in Ocean Models

Assuming unit amplitude of incoming teleseismic P wave beneath the LAB:

For model M1, the amplitude and polarity of each phase is given by:

$$P_mS = T_1^{PP}T_2^{PP}$$

$$PP_mS = \left(\prod_{i=1}^{2} T_i^{PP}\right)\mathbf{R}_3^{PP}R_2^{PS}$$

$$PS_mS = \left(\prod_{i=1}^{2} T_i^{PP}\right)\mathbf{R}_3^{PS}R_2^{SS}$$

$$P_lS = T_1^{PS}T_2^{SS}$$

$$PP_lS = \left(\prod_{i=1}^{2} T_i^{PP}\right)R_3^{PP}\mathbf{T}_2^{PP}\mathbf{R}_1^{PS}T_2^{SS}$$

$$PS_lS = \left(\prod_{i=1}^{2} T_i^{PP}\right)R_3^{PS}\mathbf{T}_2^{SS}\mathbf{R}_1^{SS}T_2^{SS}$$

using the reflection and transmission coefficients for each layer given in Text S1-A. Note that 1, 2 and 3 in the subscript of T and R indicate transmission and reflection coefficients on top of the asthenosphere, uppermost mantle and crust, respectively.

For model M2:

$$P_mS = T_1^{PP}T_2^{PS}T_3^{SS}$$

$$PP_mS = \left(\prod_{i=1}^{3} T_i^{PP}\right)R_4^{PP}\mathbf{T}_3^{PP}\mathbf{R}_2^{PS}T_3^{SS}$$

$$PS_mS = \left(\prod_{i=1}^{3} T_i^{PP}\right)R_4^{PS}\mathbf{T}_3^{SS}\mathbf{R}_2^{SS}T_3^{SS}$$

$$P_lS = T_1^{PS}T_2^{SS}T_3^{SS}$$

$$PP_lS = \left(\prod_{i=1}^{3} T_i^{PP}\right)R_4^{PP}\left(\prod_{i=2}^{3} \mathbf{T}_i^{PP}\right)R_1^{PS}\left(\prod_{i=2}^{3} T_i^{SS}\right)$$

$$PS_lS = \left(\prod_{i=1}^{3} T_i^{PP}\right) R_4^{PS} \left(\prod_{i=2}^{3} \mathbf{T}_i^{SS}\right) R_1^{SS} \left(\prod_{i=2}^{3} T_i^{SS}\right)$$

Note that 1, 2, 3 and 4 in the subscript of T and R indicate transmission and reflection coefficients on top of the asthenosphere, uppermost mantle, crust and sediment, respectively.

all bold-font reflection and transmission coefficients ($\mathbf{R}, \mathbf{T}$) indicate downgoing incidence ($\mathbf{R}^{PS}, \mathbf{T}^{SS} = \mathbf{R}^{\grave{S}\acute{P}}, \mathbf{T}^{\grave{S}\grave{S}}$), otherwise upgoing ($R^{SS}, T^{SS} = R^{\acute{S}\grave{S}}, T^{\acute{S}\acute{S}}$).

Text S2: Time Correction in the Presence of Sediments

Due to the delay effects of the sedimentary layer, the stacking and linear search technique described in section 2.x would fail if time delays associated with the sedimentary layer are not corrected for (Yeck, Sheehan, and Schulte-Pelkum 2013). Following (Yu et al. 2015), we adjust equation (6)-(7) to accommodate for the time delays:

$$\widetilde{t'}_{PmS}(p_i) = t'_{PmS}(p_i) + \delta t(p_i) \tag{S1a}$$

$$\widetilde{t'}_{PPmS}(p_i) = t'_{PPmS}(p_i) + \Delta t(p_i) - \delta t(p_i) \tag{S1b}$$

$$\widetilde{t'}_{PSmS}(p_i) = t'_{PPmS}(p_i) + \Delta t(p_i) + \delta t(p_i) \tag{S1c}$$

$$\widetilde{t}_{PPmS}(p_i) = \frac{A+B}{A-B}\left(t_{PmS}(p_i) - \delta t\right) + \Delta t(p_i) - \delta t(p_i) \tag{S2a}$$

$$\widetilde{t}_{PSmS}(p_i) = \frac{2A}{A-B}\left(t_{PmS}(p_i) - \delta t\right) + \Delta t(p_i) \tag{S2b}$$

where $\Delta t(p_i)$ and $\delta t(p_i)$ is the two-way travel time of the reverberations in the sediment and the time delay (relative to the direct P) of the *PbS* phase (Ps conversion from the bottom of sediment), respectively:

$$\Delta t(p_i) = \frac{2H_{sed}}{v_{s_{sed}}}\sqrt{1 - v_{s_{sed}}^2 p_i^2} \tag{S3a}$$

$$\delta t(p_i) = \frac{H_{sed}}{v_{s_{sed}}}\sqrt{1 - v_{s_{sed}}^2 p_i^2} - \frac{H_{sed}}{v_{p_{sed}}}\sqrt{1 - v_{p_{sed}}^2 p_i^2} \tag{S3b}$$

After the correction for the travel times associated with sediment, the station is virtually downward projected to the bottom of the sedimentary layer. The aforementioned stacking for κ and v_p and the linear search for H can then be implemented to determine the sub-sediment crustal structure.

For the linear search for the thickness of Moho to LAB, we simply modify equation (9) by substituting the Moho-associated travel times by the time-corrected ones defined in equation (S1a)-(S1c):

$$t'_1 = \widetilde{t}_{P_l S}(p_i) = \hat{\widetilde{t'}}_{P_m S}(p_i) + \frac{H_{LAB}}{\hat{v}_{p_m}}(\hat{A}_m - \hat{B}_m) \tag{S4a}$$

$$t'_2 = \widetilde{t}_{PP_l S}(p_i) = \hat{\widetilde{t'}}_{P_m S}(p_i) + \frac{H_{LAB}}{\hat{v}_{p_m}}(\hat{A}_m + \hat{B}_m) \tag{S4b}$$

Then H_{LAB} can be determined using the linear search defined in equation (8).

Figure S1

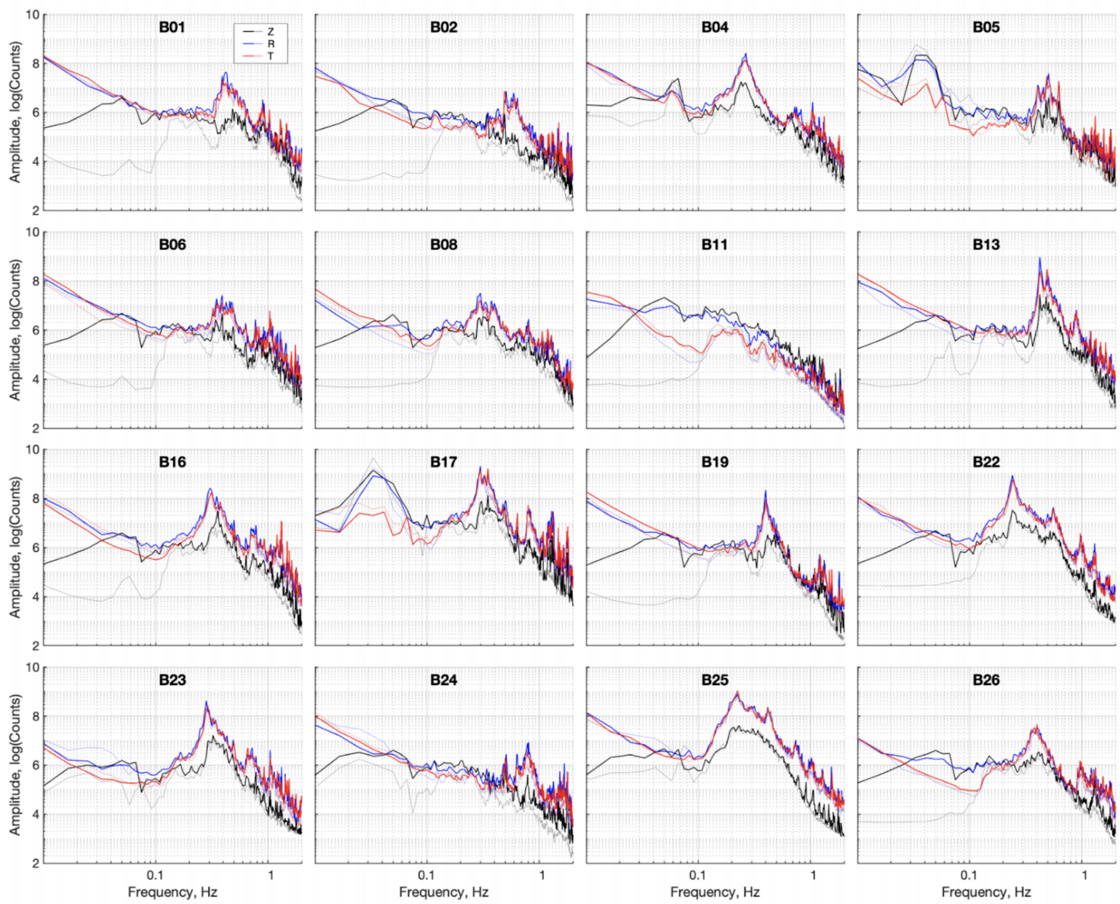

Figure S1. Mean power spectra for all events used at each station in this study. Black, blue and red lines indicate vertical, radial and transverse components, respectively; solid colors and lighter colors indicate P wave signal and pre-event noise, respectively. The spectra of P wave signal was calculated for a 120 s long time window starting 20 s before the P wave arrival; the spectra of pre-event noise was calculated for a 120 s long time window starting 180 s before the P wave arrival.

Figure S2

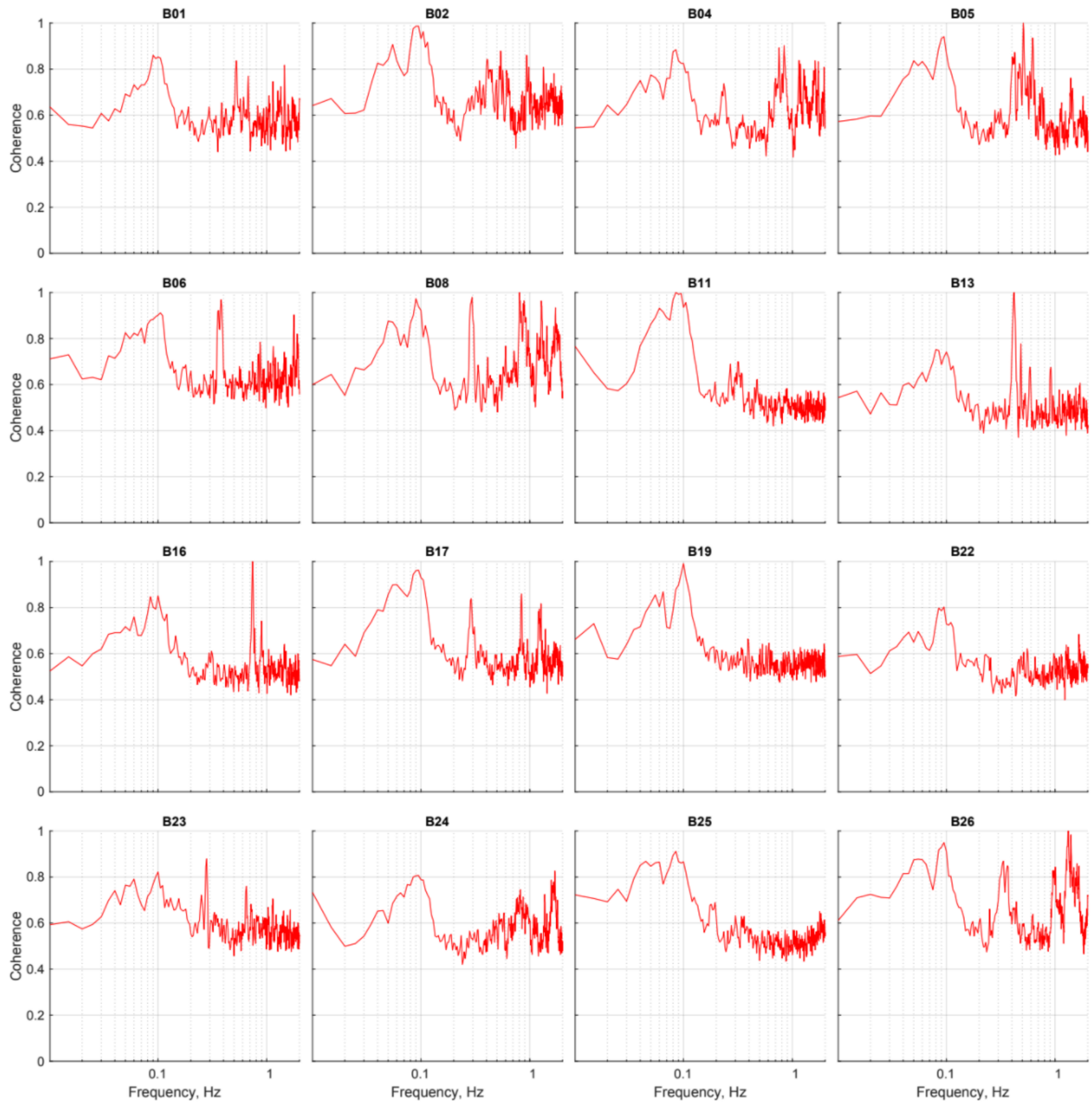

Figure S2. Average coherence between vertical (Z) and radial (R) components of all events used at each station.

TABLE

Table S1. Station information.

Station	Event No.	Latitude	Longitude	Elev. (m)	H_{Sed} (m)
B01	49	10.67°N	147.50°W	-5331.5	209.0
B02	52	11.06°N	145.71°W	-5276.5	102.0
B04	49	10.46°N	146.37°W	-5111.5	202.0
B05	42	10.78°N	144.85°W	-5196.5	178.0
B06	42	9.71°N	147.75°W	-5253.5	279.0
B08	46	8.75°N	148.00°W	-5198.5	303.0
B11	50	9.16°N	146.00°W	-4889.5	245.0
B13	46	9.25°N	145.55°W	-5174.5	239.0
B16	48	9.39°N	144.88°W	-5077.5	228.0
B17	38	9.43°N	144.65°W	-5137.5	224.0
B19	41	9.65°N	143.55°W	-5058.5	195.0
B22	38	7.81°N	145.80°W	-5220.5	277.0
B23	40	8.14°N	144.29°W	-5115.5	258.0
B24	40	8.88°N	142.91°W	-5157.5	218.0
B25	40	7.16°N	146.72°W	-5109.5	304.0
B26	42	7.54°N	144.95°W	-5042.5	278.0

*Event No. is the number of events used in RF calculation at each station; data of H_{Sed}, i.e. sediment thicknesses, comes from the GlobSed model (Straume et al., 2019).